INVESTIGATION OF INVISCID SHEAR LAYER BY LINEAR STABILITY THEORIES

A THESIS SUBMITTED TO
THE GRADUATE SCHOOL OF NATURAL AND APPLIED SCIENCES
OF
MIDDLE EAST TECHNICAL UNIVERSITY

BY

AHMET EMRE TOPBAŞ

IN PARTIAL FULFILLMENT OF THE REQUIREMENTS
FOR
THE DEGREE OF MASTER OF SCIENCE
IN
AEROSPACE ENGINEERING

JULY 2018

Approval of the thesis:

INVESTIGATION OF INVISCID SHEAR LAYER BY LINEAR STABILITY THEORIES

Submitted by **AHMET EMRE TOPBAŞ** in partial fulfillment of the requirements for the degree of **Master of Science in Aerospace Engineering Department, Middle East Technical University** by,

Prof. Dr. Halil Kalıpçılar _____
Dean, Graduate School of **Natural and Applied Sciences**

Prof. Dr. Ozan Tekinalp _____
Head of Department, **Aerospace Engineering**

Prof. Dr. Serkan Özgen _____
Supervisor, **Aerospace Engineering Dept., METU**

Examining Committee Members:

Assoc. Prof. Dr. Utku Kanoğlu _____
Aerospace Engineering Dept., METU

Prof. Dr. Serkan Özgen _____
Aerospace Engineering Dept., METU

Prof. Dr. Zafer Dursunkaya _____
Mechanical Engineering Dept., METU

Prof. Dr. Yusuf Uludağ _____
Chemical Engineering Dept., METU

Asst. Prof. Dr. Durmuş Sinan Körpe _____
Aeronautical Engineering Dept., UTAA

Date: _____

I hereby declare that all information in this document has been obtained and presented in accordance with academic rules and ethical conduct. I also declare that, as required by these rules and conduct, I have fully cited and referenced all material and results that are not original to this work.

Name, Last Name: Ahmet Emre Topbaş

Signature :

ABSTRACT

INVESTIGATION OF INVISCID SHEAR LAYER BY LINEAR STABILITY THEORIES

TOPBAŞ, Ahmet Emre
M.S., Department of Aerospace Engineering
Supervisor : Prof. Dr. Serkan Özgen

July 2018, 70 pages

In this thesis, spatial and temporal instabilities of the inviscid shear layer flows are investigated using the linear stability theory. Utilizing the small and wavy disturbances, Rayleigh equation was derived from the Helmholtz vorticity equation. For the hyperbolic-tangent velocity profile, the Rayleigh equation was solved by using space and time amplification approaches by an in-house Fortran code involving RK4 and simplex method algorithm. Eigenvalues of various disturbance frequencies were calculated both for spatial and temporal amplification theories. Results of two theories were compared and the most strongly amplified disturbance frequencies were calculated. Eigenfunctions of spatial theory were plotted for various disturbance frequencies. For the most strongly amplified disturbance frequency, eigenfunctions were calculated for both theories and compared. In spatial amplification case, derivatives of the eigenfunctions and the vorticity amplitudes were also calculated for different disturbance frequencies. By using the vorticity amplitudes, constant vorticity distributions of spatial amplification were plotted at different times in order to demonstrate the mechanism of instability. At the most strongly amplified disturbance frequency

of spatial theory, the motion of particles at different locations in the shear layer were investigated. To investigate the motions of the particles and the characteristics of the instability clearly, the pathlines and the streaklines of the disturbed shear layer were calculated and the streakline patterns were drawn. The pathlines and streaklines were also compared in terms of their ability to reflect the instability mechanism. The streaklines of the shear layer at different disturbance frequencies were compared. Results calculated by the help of the Fortran code were compared with experimental and numerical data in the literature and seen that they are in agreement. The Fortran code was also tested with the different velocity profiles to check its capability. The reasons why the code could not solve the parabolic velocity profiles were discussed.

Keywords: Shear layer, Linear Stability Theory, Boundary layer, Flow Instability, Temporal Amplification, Spatial Amplification

ÖZ

VİSKOZ OLMAYAN KESME TABAKASININ DOĞRUSAL KARARLILIK TEORİLERİ İLE İNCELENMESİ

TOPBAŞ, Ahmet Emre
Yüksek Lisans, Havacılık ve Uzay Mühendisliği Bölümü
Tez Yöneticisi : Prof. Dr. Serkan Özgen

Temmuz 2018 , 70 sayfa

Bu tezde, doğrusal kararlılık teorisi vasıtasıyla viskoz olmayan kesme tabakası akışının uzaysal ve zamansal kararsızlıkları incelenmiştir. Dalga şeklindeki küçük bozuntular kullanılarak Helmholtz girdap denkleminden Rayleigh denklemi elde edilmiştir. Hiperbolik tanjant hız profili için Rayleigh denklemi dördüncü dereceden Runge-Kutta ve simpleks method algoritmasını kullanılarak geliştirilen kod vasıtasıyla uzaysal ve zamansal genleşme yaklaşımları ile çözülmüştür. Çeşitli bozuntu frekanslarının özdeğerleri uzaysal ve zamansal genleşme için hesaplanmıştır. İki teorinin sonuçları karşılaştırılarak, en güçlü şekilde genleşen bozuntu frekansları değerlendirilmiştir. Uzaysal teorinin özfonksiyonları çeşitli bozuntu frekansları için çizdirilmiştir. En güçlü şekilde genleşen bozuntu frekansı için, her iki teorinin özfonksiyonları hesaplanmış ve karşılaştırılmıştır. Uzaysal genleşme durumunda, özfonksiyonların türevleri ve girdap genlikleri de farklı bozuntu frekansları için hesaplanmıştır. Kararsızlık mekanizmasını görselleştirebilmek için, uzaysal genleşmenin farklı zamanlardaki sabit girdap dağılımları girdap genlikleri kullanılarak çizdirilmiştir. Uzaysal teorinin

en güçlü şekilde genleşen bozuntu frekansında, kesme tabakasında değişik konumlarda bulunan parçacıkların hareketleri incelenmiştir. Parçacıkların hareketlerini ve kararsızlığın karakteristiğini açıkça inceleyebilmek için, bozuntuya maruz bırakılmış kesme tabakasının yol çizgileri ve akış çizgileri çizdirilmiştir. Yol çizgileri ve akış çizgileri de kararsızlık mekanizmasını yansıtma kabiliyetleri açısından karşılaştırılmıştır. Kesme tabakasının değişik bozuntu frekanslarındaki akış çizgileri karşılaştırılmıştır. Fortran kodu ile elde edilen sonuçlar literatürde bulunan deneysel ve sayısal veriler ile karşılaştırılmış ve sonuçların uyumlu olduğu olduğu görülmüştür. Fortran kodu kapasitesini anlayabilmek için değişik hız profilleri ile test edilmiştir. Kodun parabolik hız profillerini neden çözemediği tartışılmıştır.

Anahtar Kelimeler: Kesme Tabakası, Doğrusal Kararlılık Teorisi, Sınır Tabakası, Akış Kararsızlığı, Zamansal Genleşme, Uzaysal Genleşme

To my family

ACKNOWLEDGMENTS

I would like to express my deepest appreciation to my supervisor Prof. Dr. Serkan Özgen for his support, guidance and wise advices throughout the thesis.

I want to emphasize my special thanks to Merve Okatan for her endless support, trust and encouragement. I always consulted her first, whenever I need.

I would like to thank to my friends Kıvanç Arslan and Başak Bingöl for their help and advice during the thesis.

Finally, I am very thankful to my parents Mr. Eriman Topbaş, Mrs. Emine Topbaş, my sisters Mrs. Elif Neslihan Akdemir and Mr. Esra Topbaş for their help, motivation and endless love.

TABLE OF CONTENTS

LIST OF TABLES

TABLES

LIST OF FIGURES

FIGURES

LIST OF ABBREVIATIONS

1-D	One dimensional
2-D	Two dimensional
3-D	Three dimensional
RK4	Fourth order Runge-Kutha

CHAPTER 1

INTRODUCTION

Boundary layer concept was first presented by Ludwing Prandtl at the Third International Congress of Mathematicians in 1904 [1]. In his paper "On the motion of a fluid with very small vicosity" -published in the proceedings of Congress- Prandtl defined the most important aspect about the fluid flow with small viscosity as the characteristics of the fluid at the wall of the solid boundary. He pointed that the viscosity was the reason for the no-slip condition at the wall, and the effect of the viscosity experienced in a thin region near the surface. He usually used the term "transition layer" instead of "boundary layer" for this region in his paper, but "boundary layer" term became more popular after. Effect of the viscosity was ignorable outside the boundary layer in the Prandtl's concept meaning that the fluid had inviscid characteristics.

In fluid mechanics, boundary layer is thin layer of flow over a solid surface in which the fluid velocity changes from an upstream value to zero velocity at the surface. Therefore, viscous shear stresses are effective due to the velocity gradient. The flow within the boundary layer may be laminar or turbulent. Generally, the flow in boundary layers are laminar at the upstream portion and turbulent in the downstream.

There is also a different type of boundary layer, which are independent of solid boundaries, occurring at jets or wakes. These are called free boundary layers or shear layers which is the main point of focus of this thesis. Shear layers or the flows involving them appears in various industry applications; for example, widely-used multi-element airfoils of passenger aircraft, still under development scramjet engines, etc.

The flow structure of the shear flows directly affects the performance of the system that contains them. Depending on the application, laminar, turbulent or transient shear

flows may be preferred. Therefore, the shear flow phenomena have been continously analyzed by different researchers in terms of its instability characteristics.

1.1 Laminar and Turbulent Boundary Layers

If the fluid particles in the flow move in smooth layers, then it is called as laminar flow. In a turbulent flow the fluid particles moves in random directions due to the velocity fluctuations along the directions [2]. In Figure 1.1, laminar, turbulent and transition from laminar to turbulent flow in a boundary layer over a plate can be seen [3].

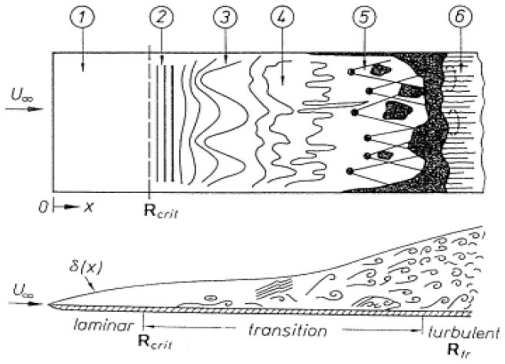

Figure 1.1: Stages of Laminar-Turbulent Transition in a Boundary-Layer

In this figure numbers are showing;

1. Stable, laminar flow following the leading edge,
2. Unstable, laminar flow with 2-D Tollmien-Schlichting waves,
3. Development of unstable, laminar, 3-D waves and vortex formation,
4. Burst of turbulence in places of very high local vorticity,
5. Formation of turbulent spots in places where the turbulent velocity fluctuations are large,
6. Coalescence of turbulent spots into a fully developed turbulent boundary layer.

the steps given above are not must-have criteria for the laminar to the turbulent transition. There are also some mechanisms that can make transition sequence shorter by allowing skip of one or more of transition steps (numbered from 2 to 5). These mechanisms are called as by-pass mechanisms, and they can be preset due to either natural reasons or artificial tools.

The natural by-pass mechanisms are;

- Görtler vortices,
- Surface roughness,
- Freestream turbulence and noise,

which are briefly described below.

Görtler vortices: Görtler vortices are secondary flows which occur along concave surfaces. The Görtler vortices and mechanism for their formation is illustrated in Figure 1.2. As seen from Figure 1.2, centrifugal force due to concave surface acts

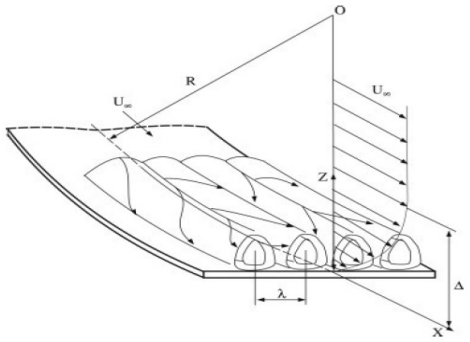

Figure 1.2: Formation of Görtler Vortices

in the direction of smaller velocity. In consequence, the particles located relatively above have higher velocities and lower radius of rotation. Thus, they are subjected to greater centrifugal forces compared to the particles below them. Heavier fluid flowing over a lighter fluid (like a water-oil flow) can be an analogy for the situation. Then particles under the effect of greater centrifugal forces penetrate into the particles

subject to smaller centrifugal forces. Peak and valley structures of Görtler vortices occur even before 2-D Tollmien-Schlichting waves (Step 2 in Figure 1.1) and 3-D vortex formation takes precedence immediately.

Surface roughness: Since surface roughness is a source for disturbances in the flow, it has direct impact on the laminar turbulent transition. If an isolated roughness element on the surface is considered, there is a critical roughness height, k_{crit}, which changes according to shape of the roughness element, the external velocity distribution, location of the roughness element on the body and the flow velocity. Below this k_{crit} value, the roughness element has no effect on the laminar turbulent transition. In other words, the transition location on a smooth surface can only change, if the surface roughness element height is greater than k_{crit} value. There is also a second critical roughness element value, k^*_{crit}, when the height of the roughness element increases beyond of it, the transition takes places just downstream of the roughness element.

Freestream turbulence and noise: Intensity of freestream turbulence is proportional to the disturbance velocities in the flow and inversely proportional to the freestream velocity. The transition Reynolds number is an indicator of the effect of the turbulence intensity. As the freestream turbulence intensity decreases, the Reynolds number at which the transition occurs increases. However, there is a threshold value for the decrease of the intensity. Below this threshold value, it is not possible to delay the transition further.

In addition to natural by-pass mechanisms described above, there are artificial by-pass mechanisms which are used as tools for intentional fluid control. For artificial by-pass mechanisms, vibrating ribbon and pneumatic turbulator can be given as examples.

1.2 LinearStability Theory

Linear stability theory can be described as superimposition of the small disturbances onto the undisturbed boundary layer state and then checking whether the disturbances

amplify or not in brief [3]. The flow is termed stable if the disturbances do not grow. Otherwise, the flow is unstable. A more stable basic state created by flow control may delay the transition from laminar to turbulent flow. Just mentioned in the previous section, with the use of artificial by pass-mechanisms the transition can be made faster also. Linear stability analysis is performed locally by linearizing the complete unsteady Navier-Stokes equations about the basic state (the undisturbed boundary layer state) of the boundary layer. It is assumed that the flow in the basic state is locally parallel to the boundary (i.e. wall). The parallel-flow assumption is a good approximation to the linearized Navier-Stokes equations since the nonparallel effects are negligible. By superposing small disturbances q' onto the basic state Q, the stability equations giving the total flow quantities q are obtained. The basic state involves the chordwise, normal-to-the-wall and spanwise velocities, as well as pressure and temperature.

$$q(x, y, z, t) = Q(y) + q'(x, y, z, t) \tag{1.1}$$

The flow quantities q and Q separately satisfy the Navier-Stokes equations; however, the disturbance quantities q' do not. The equations of q in terms of only the disturbance quantities q' are obtained by dropping the basic state terms. In addition, the disturbance equations are linearized by neglecting the small terms (i.e. products of q'). Disturbance equations become linear and the coefficients depend on y distance only. Therefore, in order to reduce the disturbance equations to ordinary differential equations, exponential solutions in terms of the independent variables (x, z, t) are employed. The solution can be generalized as given below;

$$q' = q_0(y)exp(i\Theta) + c.c. \tag{1.2}$$

In this equation, $\Theta(x, z, t)$ is the phase function and the term $c.c.$ denotes the complex conjugate. The system of these equations is simply an eigenvalue problem for $q_0(y)$. The eigenfunctions are modes of the system. For incompressible streamwise instabilities, the most unstable mode is termed as the first mode. Moreover, there is only one unstable mode for this type of flow. When other types of flows are considered just like the compressible flows, there can be more unstable modes than one. The classification of disturbances are made according to their amplification characteristics. Two kinds of the amplification exist for the disturbances; spatial amplification

and temporal amplification. In the spatial amplification, disturbance frequency is real, and the wavenumbers assumed to be complex. The real parts of the wavenumbers are physical wavenumbers. The imaginary parts of the wavenumbers show the amplification rates of the disturbances. On the contrary, the wavenumbers of the disturbances are assumed to be real and the frequency is complex for the temporal amplification approach. There is also both temporal and spatial amplification case. In this situation, all of the parameters of the amplification approach are assumed to be complex [4].

1.3 Aspects of Stability Theory

In the previous section, a general methodology of the stability theory was explained. In this section, general elements of the stability theory is introduced below [3];

- The stability theory is concerned with individual sine waves propagating in the boundary-layer, parallel to the wall (i.e. parallel mean flow $U = U(y)$ and $V = 0$).
- Amplitudes of the waves vary through the boundary-layer and are small enough so that linear theory may be used.
- Frequency of a wave is denoted by ω.
- λ indicates the wavelength, and the corresponding wave number can be calculated as $\alpha = 2\pi/\lambda$.
- α is the wavenumber of the disturbances in the chordwise, while β is the wavenumber of the disturbances in the spanwise direction.
- 2-D waves are the lines of constant phase normal to the freestream direction. Streamwise instabilities of a swept wing can be predicted by streamwise traveling waves that appear in 2-D boundary layers in the midchord region of swept wings. 2-D waves can be observed as secondary instabilities of a flow with stationary streamwise vortex structures, also [4].

- Oblique waves are the instability waves with the wavenumbers defined by vectors.
- Phase velocity is termed by c which is lower than the freestream velocity U_∞
- In the boundary-layer, there is a point where the mean flow velocity is equal to phase velocity. This region is called as the critical layer. Disturbance wave amplitude usually gets its maximum near the critical layer.
- Numerical results calculated from stability theory are usually presented in a $Re - \alpha$ space for viscous flow. There is a critical Reynolds number below which no amplification is possible.
- If a wave is introduced into a steady boundary-layer with a specific frequency, as the wave propagates downstream the frequency of the wave will be protected while the wave number will change.

With the elements the stability theory contains, the theory can be used to calculate;

- Amplification and damping rates of the disturbances,
- Frequency, wavenumber and Reynolds number of the instability waves,
- Amplitude history of a constant frequency wave as it travels through the unstable region,
- Given some initial disturbance spectrum, it is possible to identify the frequency whose amplitude has increased the most at each Reynolds number. Among the spectrum, most probably there is a specific disturbance, that triggers the whole transition process after reaching a critical amplitude.

1.4 Inviscid Instability

In the absence of viscosity meaning that Reynolds number is infinite, the governing disturbance equation for the instability waves is the Rayleigh equation [4]. While

analyzing the inviscid case for the boundary layer instabilities the effect of the vicosity is restricted to establish the basic-state velocity profile, the impact on the disturbances is neglected.

Another important point for the inviscid instabilities is Rayleigh's inflection theorem. It states that if a boundary layer flow is unstable, then the velocity profile in the boundary layer has an inflection point. It can be re-stated mathematically as if $U(y)''$ does not change sign inside the boundary layer, then amplification rates $\alpha_i > 0$ or $c_i < 0$ depending on the which type of amplification (i.e.spatial or temporal) is employed. In Figure 1.3, (a) indicates a velocity profile without an inflection point, while the velocity profiles given in (b) and (c) show the ones that have inflection points, therefore are unstable according to Rayleigh's inflection point theorem.

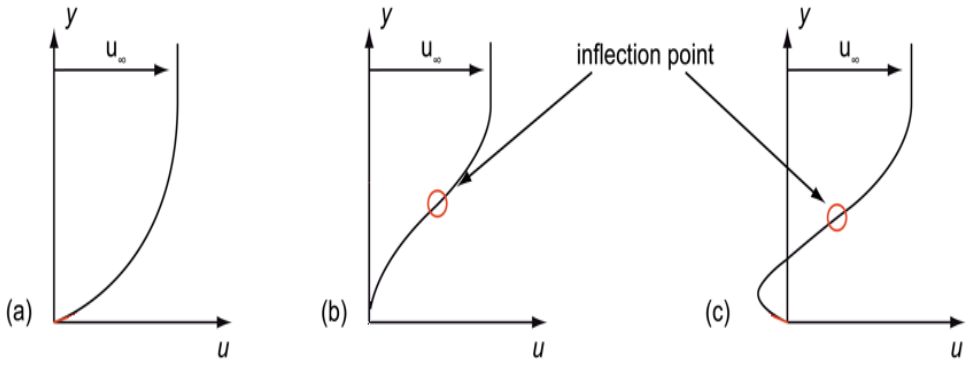

Figure 1.3: Velocity profiles with/without inflection points

1.5 Literature Survey

Rayleigh [5] showed for inviscid fluids, velocity profiles having inflection points are unstable when they are exposed to wavy disturbances. Since the shear layer flow at large Reynolds numbers is almost parallel and instability mechanism of the shear layer is inviscid, the inviscid linearized stability theory of unidirectional flow can be applied for shear layers for high Reynolds numbers.

For large Reynolds numbers, it was shown by Lessen [6], Esch [7] and Betchov &

Szewczyk [8] that the inviscid theory could calculate the asymptotical neutral curve and the amplification of disturbances gets smaller values compared to inviscid flow for finite Reynolds numbers. These were also proven by Tatsumi & Kakutani [9] for a plane jet.

Sato [10] verified by experiments that at high Reynolds numbers, viscosity has little effect on the shear layers of a two-dimensional jet. For axisymmetric jets, experiments conducted by Schade-Michalke [11] and Michalke-Wille [12] showed similar results with Sato [10].

Sato [13] used artificial disturbances to investigate shear layers by experiments. To compare the results with the inviscid linearized stability theory which depends on the solution of the Orr-Sommerfeld equation, Sato [14] used the disturbance phase velocity. By the help of the phase velocity, he could manage the temporal to spatial transformation of the disturbance growth rates. Moreover, Sato [14] experienced a phase reversal of the flow away from the critical layer.

Similar velocity fluctuations were also discovered by Wehrmann & Wille [15]. This distribution of velocity fluctuation was explained with the existence of ring vortices in the jet boundary layer.

To explain the formation of vortices in free boundary layers by the linearized stability theory, many attempts were made. Michalke [16] used the hyperbolic-tangent velocity profile which was very close to the jet-boundary layer velocity profiles to explain the phenomena. However, since he used temporal amplification approach, the results did not agree well with the experimental ones conducted by Freymuth [17]. To get a better description of shear layer instability, Michalke [18] later used spatial theory and found that the growth of disturbances in a free boundary layer can be calculated more accurately by the spatial theory.

Yang & Zhou [19] stated the initial development of the shear layer can be predicted from linear stability theory. Results obtained by Michalke [18] are beneficial to validate the numerical solvers of the inviscid linearized stability as Liu, Wang & Piao [20] did.

Özgen & Uzol [21] investigated the instability characteristics of an electrified liquid jet discharging from a nozzle into a stagnant gas by using the linear stability theory. They used parabolic velocity profiles and made an inviscid analysis by using the cylindrical momentum equations.

1.6 Contribution of This Thesis

In this thesis, to develope a Fortran Code to analyze the spatial and temporal instabilities for inviscid shear layers is aimed. To achieve this the linear stability theory used. Rayleigh and Ricatti equations were derived from the Helmholtz vorticity equation by using the small and wavy disturbances. In-house Fortran Code involving Runge-Kutta-Gill and simplex method algorithms were used to investigate the hyperbolic tangent velocity profile with two different amplification approaches.

By using the Fortran code developed, eigenvalues of various disturbance frequencies were calculated for both spatial and temporal amplification. Validation of the code was achieved by comparison of the eigenvalues obtained by the code with the results given in the literature.

A comparison between the results obtained by the code with the spatial and temporal theories is also performed. The results of two approaches were checked on whether they could achieve similar results with the experimental ones. The investigation of the eigenfunctions and their derivatives also helped to make a distinction between two theories.

Results of the code are visualized with the post-processing tools developed. Basically, these post processing tools were used to calculate the vorticity amplitudes and the constant vorticity distributions, the pathlines and the streaklines of the inviscid shear flow. The post-processing tools were also verified by the literature results. After the validation of the post-processing tools, the results were examined to understand the instability mechanism. In addition, which method was more suitable to visualize the flow was determined.

The code was run with different velocity profiles were analyzed. The reason why the code was not capable of analyzing the inviscid parabolic velocity profiles are discussed.

1.7 Organization of the Thesis

The organization of this thesis is as follows. Boundary layers, laminar and turbulent flows are briefly introduced in Chapter 1. Basics of linear stability theory and its mathematical framework are also given in this section. Specific points of inviscid stability theory, and related literature to it are set in Chapter 1.

Chapter 2 involves the detailed mathematical background for the Fortran code developed to investigate the inviscid shear layers. Derivations of Rayleigh and Ricatti equations for specific velocity profiles are made, and Runge-Kutta-Gill method and Simplex Method employed in the Fortran code are explained in Chapter 2. Chapter 2 also includes the methodology of the necessary post-processing tools of the developed Fortran code to visualize the results of it.

Validation of the developed Fortran code is done in Chapter 3 by using a hyperbolic velocity profile that have both experimental and analytical results in the literature. Results of the Fortran code and the literature results are compared in the same section.

In Chapter 4, the Fortran code is used to analyze the different velocity profiles and the differences in the results of the Fortran code and the analysis in the literature is discussed.

Finally, in Chapter 5 thesis is finalized with concluding remarks and recommendations for future studies.

CHAPTER 2

METHODOLOGY

2.1 Derivation of the Rayleigh Equation

To understand the mechanism of instabilities more deeply, Rayleigh's linearized equation is derived based on the small and wavy disturbances. Rayleigh used the Helmholtz' s vorticity equation, instead of Navier-Stokes equations to model the inviscid shear layers. Helmholtz's vorticity equation defines the change in the vorticity in two-dimensional flow as;

$$\frac{d\Omega}{dt} = \frac{\partial\Omega}{\partial t} + u\frac{\partial\Omega}{\partial x} + v\frac{\partial\Omega}{\partial y} = 0 \tag{2.1}$$

In this equation Ω denotes the vorticity vector, and u(x,y,t) and v(x,y,t) are the x- and y- components of the velocity vector **c**, respectively. Vorticity can be defined as curl of the velocity vector. Then, the velocity vector and its relation with the vorticity can be stated as below;

$$\mathbf{c} = (u, v, 0) \tag{2.2}$$

$$curl\ \mathbf{c} = (0, 0, \Omega) \tag{2.3}$$

Taking the curl of the given velocity vector, the vorticity becomes:

$$\Omega = \frac{\partial v}{\partial x} - \frac{\partial u}{\partial y} \tag{2.4}$$

Assuming a unidirectional steady mean flow, which has a velocity profile given as $U(y)$, the vorticity distribution of this mean flow is denoted by Ω_0, where the differ-

entiation is taken with respect to y:

$$\Omega_0 = -U' \tag{2.5}$$

By superimposing a small disturbance upon this basic flow equations (2.6) to (2.8) are obtained. In these equations ϵ denotes the magnitude of the disturbance.

$$u(x, y, t) = U(y) + \epsilon u_1(x, y, t) \tag{2.6}$$

$$v(x, y, t) = \epsilon v_1(x, y, t) \tag{2.7}$$

$$\Omega = \Omega_0 + \epsilon\Omega_1(x, y, t) \tag{2.8}$$

Substituting these three equations above into the Helmholtz vorticity equation, the following equation is obtained.

$$\frac{\partial(\Omega_0 + \epsilon\Omega_1)}{\partial t} + (U + \epsilon u_1)\frac{\partial(\Omega_0 + \epsilon\Omega_1)}{\partial x} + \epsilon v_1\frac{\partial(\Omega_0 + \epsilon\Omega_1)}{\partial y} = 0 \tag{2.9}$$

It is known from equation (2.5) that $\partial\Omega_0\backslash\partial t$ term is equal to zero and $\partial\Omega_0\backslash\partial y = -U''$. Moreover, $\partial\Omega_0\backslash\partial x = 0$ due to unidirectional steady flow parallel to the wall assumption. Then equation [2.9] becomes:

$$\frac{\partial\epsilon\Omega_1}{\partial t} + (U + \epsilon u_1)\frac{\partial\epsilon\Omega_1}{\partial x} + \epsilon v_1(-U'' + \frac{\partial\epsilon\Omega_1}{\partial y}) = 0 \tag{2.10}$$

To make further simplification, the small terms (i.e. products of the disturbance terms) can be neglected.

$$U >> | \epsilon u_1 |; | U'' | >> | \frac{\partial\epsilon\Omega_1}{\partial y} | \tag{2.11}$$

$$\frac{\partial\epsilon\Omega_1}{\partial t} + \epsilon U\frac{\partial\Omega_1}{\partial x} + \epsilon^2 u_1\frac{\partial\Omega_1}{\partial x} - \epsilon v_1 U'' + \epsilon^2 v_1\frac{\partial\Omega_1}{\partial y} = 0 \tag{2.12}$$

By eliminating the magnitude of the disturbance ϵ after neglecting the small terms in accordance with equation (2.11), we obtain equation (2.11). Equation (2.13) is the linearized disturbance equation and its solution does not depend on ϵ anymore.

$$\frac{\partial\Omega}{\partial t} + U\frac{\partial\Omega_1}{\partial x} - v_1 U'' = 0 \tag{2.13}$$

A stream function $\psi_1(x, y, t)$ can be defined satisfying the continuity equation for the disturbance velocities as follows;

$$u_1 = \frac{\partial \psi_1}{\partial y} \tag{2.14}$$

$$v_1 = -\frac{\partial \psi_1}{\partial x} \tag{2.15}$$

If only wavy disturbances are considered, disturbances in terms of stream and vorticity functions become;

$$\psi_1(x, y, t) = R\{\phi(y)e^{i(\alpha x - \beta t)}\} \tag{2.16}$$

$$\Omega_1(x, y, t) = R\{\omega(y)e^{i(\alpha x - \beta t)}\} \tag{2.17}$$

Where α denotes wave number and β shows the frequency of the disturbance. By using equations (2.14) and (2.15) wavy disturbance expressions given above can be inserted into the linearized disturbance equation (2.13). Moreover, if we put these wavy disturbance equations into equation (2.1), the following equations are obtained.

$$u_1 = \frac{\partial \psi_1}{\partial y} = \frac{\partial(\phi e^{i\alpha x - i\beta t})}{\partial y} = \phi' e^{i\alpha x - i\beta t} \tag{2.18}$$

$$v_1 = -\frac{\partial \psi_1}{\partial x} = -\frac{\partial(\phi e^{i\alpha x - i\beta t})}{\partial x} = -ie^{i\alpha x - i\beta t}\alpha\phi \tag{2.19}$$

$$\frac{\partial \Omega_1}{\partial t} = \frac{\partial(\omega e^{i\alpha x - i\beta t})}{\partial t} = -ie^{i\alpha x - i\beta t}\beta\omega \tag{2.20}$$

$$\frac{\partial \Omega_1}{\partial x} = -\frac{\partial(\omega e^{i\alpha x - i\beta t})}{\partial x} = ie^{i\alpha x - i\beta t}\alpha\omega \tag{2.21}$$

The linearized disturbance equation, equation (2.13) becomes:

$$-ie^{i\alpha x - i\beta t}\beta\omega + Uie^{i\alpha x - i\beta t}\alpha\omega + ie^{i\alpha x - i\beta t}\alpha\phi U'' = 0 \tag{2.22}$$

By eliminating the term $ie^{i\alpha x - i\beta t}$, we get;

$$-\beta\omega + U\alpha\omega + \alpha\phi U'' = [\alpha U - \beta]\omega + \alpha U''\phi = 0 \tag{2.23}$$

The vorticity equation (equation (2.4)) in terms of the velocity components becomes:

$$\frac{\partial v}{\partial x} = -ie^{i\alpha x - i\beta t}\alpha^2\phi = e^{i\alpha x - i\beta t}\alpha^2\phi \tag{2.24}$$

$$-\frac{\partial u}{\partial y} = -\phi'' e^{i\alpha x - i\beta t} \tag{2.25}$$

$$\omega e^{i(\alpha x - \beta t)} = e^{i\alpha x - i\beta t}\alpha^2\phi - \phi'' e^{i\alpha x - i\beta t} \tag{2.26}$$

Eliminating the $e^{i\alpha x - i\beta t}$ term from the both side of the equality and by re-arrengement of the terms, equation given below is obtained.

$$\omega = -[\phi'' - \alpha^2\phi] \tag{2.27}$$

Equation (2.27) can be used to eliminate ω term in equation (2.23).

$$-[\alpha U - \beta][\phi'' - \alpha^2\phi] + \alpha U''\phi = 0 \tag{2.28}$$

Dividing each term by α and multiplying with -1, Rayleigh equation given below is obtained.

$$(U - \beta/\alpha)[\phi'' - \alpha^2\phi] - U''\phi = 0 \tag{2.29}$$

For unbounded velocity profiles, the disturbances must vanish at infinity. Therefore, our boundary conditions are defined given by equation (2.30):

$$\phi(+\infty) = \phi(-\infty) = 0 \tag{2.30}$$

Since the velocity profile is unbounded;

$$\lim_{y \to \pm\infty} U'' = 0 \tag{2.31}$$

while $y \to \pm\infty$, Rayleigh equation should be equal to zero also; therefore, equation (2.29) becomes as below considering that U'' is equal to zero:

$$(U - \beta/\alpha)[\phi'' - \alpha^2\phi] = 0 \tag{2.32}$$

In order to satisfy the equality, $[\phi'' - \alpha^2\phi]$ term should be zero. Then:

$$\phi'' - \alpha^2\phi = 0 \tag{2.33}$$

The characteristic equation of the homogeneous equation given by equation (2.33) is given by equation (2.34).

$$r^2 - \alpha^2 r = 0 \tag{2.34}$$

The nontrivial roots of this equation are $r_1 = +\alpha$ and $r_2 = -\alpha$. The general solution of equation (2.34) and the derivatives of it can be written as below;

$$\phi = c_1 e^{\alpha y} + c_2 e^{-\alpha y} \tag{2.35}$$

$$\phi' = c_1 \alpha e^{\alpha y} - c_2 \alpha e^{-\alpha y} \tag{2.36}$$

$$\phi'' = c_1 \alpha^2 e^{\alpha y} + c_2 \alpha^2 e^{-\alpha y} \tag{2.37}$$

As $y \to -\infty$, term $c_1 e^{\alpha y}$ equals to zero, so c_2 should be equal to zero in order to satisfy the boundary condition given in equation (2.30):

$$\phi = c_2 e^{-\alpha y} = 0 \tag{2.38}$$

$$c_2 = 0 \tag{2.39}$$

Then, ϕ and its first derivative can be written as below:

$$\phi = c_1 e^{\alpha y} \tag{2.40}$$

$$\phi' = c_1 \alpha e^{\alpha y} = \alpha\phi \tag{2.41}$$

Similary, at $y = \infty$, term $c_2 e^{-\alpha y}$ equals to zero, so c_1 should be equal to zero in order to satisfy the boundary condition given in equation (2.30):

$$\phi = c_1 e^{\alpha y} = 0 \tag{2.42}$$

$$c_1 = 0 \tag{2.43}$$

Then, ϕ and its first derivative can be written as below:

$$\phi = c_2 e^{-\alpha y} \tag{2.44}$$

$$\phi' = -c_1 \alpha e^{-\alpha y} = -\alpha \phi \tag{2.45}$$

Therefore, the boundary conditions of the first derivative of ϕ at $y \to \pm\infty$ can be stated as;

$$\phi'(+\infty) = -\alpha \phi(-\infty) \tag{2.46}$$

$$\phi'(-\infty) = \alpha \phi(-\infty) \tag{2.47}$$

To solve the Rayleigh equation numerically, the order of the equation should be reduced using the definition $\phi = exp[\int \Phi dy]$.

$$\phi = e^{\int \Phi dy} \tag{2.48}$$

$$\phi' = \Phi e^{\int \Phi dy} \tag{2.49}$$

$$\phi'' = \Phi^2 e^{\int \Phi dy} + \Phi' e^{\int \Phi dy} \tag{2.50}$$

By putting three equations given above to Rayleigh equation, we obtain:

$$(U - \beta/\alpha)[\Phi^2 e^{\int \Phi dy} + \Phi' e^{\int \Phi dy} - \alpha^2 e^{\int \Phi dy}] - U'' e^{\int \Phi dy} = 0 \tag{2.51}$$

Eliminating the common term $e^{\int \Phi dy}$ from the equation above;

$$(U - \beta/\alpha)[\Phi^2 + \Phi' - \alpha^2] - U'' = 0 \tag{2.52}$$

By re-arranging the terms of equation (2.52), Ricatti equation is obtained given by equation (2.52) and equation (2.53) after re-arranging:

$$\Phi' = \frac{U''}{U - \beta/\alpha} + \alpha^2 - \Phi^2 \tag{2.53}$$

$$\Phi' = \alpha^2 - \Phi^2 + U''/(U - \beta/\alpha) \tag{2.54}$$

The boundary conditions of Rayleigh Equation should be adapted to Ricatti Equation. At $y \to +\infty$;

$$\Phi e^{\int \Phi dy} = -\alpha e^{\int \Phi dy} \tag{2.55}$$

At $y \to -\infty$;

$$\Phi e^{\int \Phi dy} = \alpha e^{\int \Phi dy} \tag{2.56}$$

By eliminating the common term $e^{\int \Phi dy}$ from the equations above, the boundary conditions of Ricatti equations given below is obtained.

$$\Phi(+\infty) = -\alpha \qquad \Phi(-\infty) = +\alpha \tag{2.57}$$

The mean velocity profile investigated by Michalke [16], [18] with temporal and spatial approaches is shown below by Figure 2.1. In order to validate the developed Fortran code, this velocity profile was chosen.

The velocity profile given in Figure 2.1 is a hyperbolic-tangent velocity profile which is mathematically expressed by equation (2.58).

$$U(y) = 0.5[1 + tanh(y)] \tag{2.58}$$

In the study of Michalke [18], the wave number is denoted by α. Instead of using β as wavenumber in spanwise direction, β indicates cyclic frequency in the paper of Michalke [18]. To be compatible with Michalke, in this thesis β is used as the frequency also. The wave number α and the frequency β are generally complex, where imaginary parts represent the spatial and temporal growth rates, respectively.

$$\alpha = \alpha_r + i\alpha_i \qquad\qquad \beta = \beta_r + i\beta_i \tag{2.59}$$

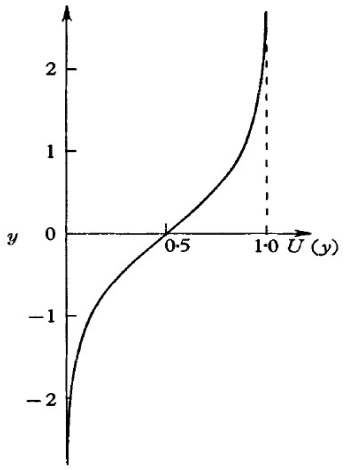

Figure 2.1: Hyperbolic Tangent Velocity Profile

For time amplification case;

$$\alpha_i = 0 \tag{2.60}$$

For space amplification case;

$$\beta_i = 0 \tag{2.61}$$

Both case have same solution when $\alpha_i = \beta_i = 0$. In this study, first spatial approach is conducted to obtain the eigenvalues of the Ricatti equation. For spatial amplification case, we have to solve an eigenvalue problem in order to determine;

$$\alpha = \alpha(\beta) = \alpha_r + i\alpha_i \tag{2.62}$$

Then by using the phase velocity c, the eigenvalues of the temporal amplification case were obtained. In order calculate the complex eigenvalues by using Ricatti equation (equation (2.54)) with its boundary conditions (equation (2.57)), a new independent variable must be defined as;

$$z = tanh(y) \tag{2.63}$$

Then hyperbolic-tangent velocity profile and its first and second derivatives can be re-stated as given below;

$$U(z) = 0.5[1 + z] \tag{2.64}$$

$$U'(y) = 0.5sech^2(y) \tag{2.65}$$

$$U''(y) = -tanh(y)sech^2(y) \tag{2.66}$$

In trigonometrics, $sech^2(y)$ equals to $1 - tanh^2(y)$. Therefore, equation (2.66) can be re-written as;

$$U''(y) = -tanh(y)[1 - tanh^2(y)] \tag{2.67}$$

With the new variable $z = tanh(y)$;

$$U''(z) = -z[1 - z^2] \tag{2.68}$$

To convert Ricatti equation to new variable z, following steps are followed.

$$\frac{dz}{dy} = \frac{1}{cosh^2(y)} = sech^2(y) = 1 - z^2 \tag{2.69}$$

$$\frac{dy}{dz} = \frac{1}{1 - z^2} \tag{2.70}$$

$$\frac{d\Phi}{dy} = \alpha^2 - \Phi^2 + \frac{U''}{U - \beta/\alpha} \tag{2.71}$$

$$\frac{d\Phi}{dz} = \frac{d\Phi}{dy}\frac{dy}{dz} = \frac{\alpha^2}{1 - z^2} - \frac{\Phi^2}{1 - z^2} + \frac{U''}{(U - \beta/\alpha)(1 - z^2)} \tag{2.72}$$

In equation (2.72), the velocity profile and its second derivative can be stated in terms of z, also. Equation (2.72) becomes, then as given below.

$$\frac{d\Phi}{dz} = \frac{\alpha^2 - \Phi^2}{1 - z^2} + \frac{-z[1 - z^2]}{(0.5[1 + z] - \beta/\alpha)(1 - z^2)} \tag{2.73}$$

By eliminating the $(1 - z^2)$ from both the denominator and the numerator of the second term of equation (2.73) and dividing both of them by 0.5, we obtain;

$$\frac{d\Phi}{dz} = \frac{\alpha^2 - \Phi^2}{1 - z^2} - \frac{2z}{(1 + z - 2\beta/\alpha)} \tag{2.74}$$

To convert the boundaries to the new variable, $z = tanh(y)$;

$$y = \pm\infty \tag{2.75}$$

$$z_b = tanh(\infty) = 1 \tag{2.76}$$

$$z_b = tanh(-\infty) = -1 \tag{2.77}$$

Then from equation (2.57);

$$\Phi(z_b) = -\alpha \qquad\qquad z_b = 1 \tag{2.78}$$

$$\Phi(z_b) = \alpha \qquad\qquad z_b = -1 \tag{2.79}$$

They can be re-stated in the form of;

$$\Phi(z_b) = -z_b\alpha \qquad\qquad z_b = \pm 1 \tag{2.80}$$

To obtain eigenvalues of spatial theory, equation (2.74) is integrated for specific β values. Starting from its boundaries towards $z = 0$ by forward and backward RK4 procedure (Runge-Kutta-Gill procedure given in Section 2.2) with an integration step $\mid \Delta z \mid = 0.025$. At z=0, the difference between the results of forward and backward RK4 integration is evaluated for different α values. To minimize the difference, 2-D Simplex method (1-D Simplex was used for timewise amplification approach is utilized. Simplex methodology is explained in Section 2.3.) is used.

The most challenging point of RK4 integration process is calculating the Φ values just one step after the boundaries. At these points, second order Taylor series expansion is used instead of RK4 since equation (2.74) does not allow calculating Φ values due to reasons explained below.

Third order Taylor series of Φ function which is expanded about $z = z_b$ can be written as;

$$\Phi(z) = \Phi(z_b) + \Phi'(z_b)(z - z_b) + \frac{\Phi''(z_b)}{2!}(z - z_b)^2 + \frac{\Phi'''(z_b)}{3!}(z - z_b)^3 \tag{2.81}$$

To evaluate this Taylor expansion, $\Phi(z_b)$, $\Phi'(z_b)$, $\Phi''(z_b)$ and $\Phi'''(z_b)$ terms should be calculated. It is already known from equation (2.80) that $\Phi(z_b)$ equals to $-z_b\alpha$. However, at the boundaries the first, the second and the third derivatives of the $\Phi(z_b)$ function can not be calculated, since they result in indeterminate forms, $(i.e. 0/0)$. Therefore, in the Taylor series expansion of $\Phi(z)$, second, third and fourth terms are calculated with the help of L'Hospital Rule.

$\Phi'(z_b)$ is written in limit form as:

$$\Phi'(z_b) = \lim_{z \to z_b} \frac{\Phi(z) - \Phi(z_b)}{z - z_b} = \frac{\alpha^2 - \Phi^2(z_b)}{1 - z_b^2} - \frac{2z_b}{(1 + z_b - 2\beta/\alpha)} \tag{2.82}$$

$$\frac{\alpha^2 - \Phi^2(z_b)}{1 - z_b^2} - \frac{2z_b}{(1 + z_b - 2\beta/\alpha)} = \frac{\alpha^2 - \alpha^2}{1 - (\pm 1)^2} - \frac{2z_b}{(1 + z_b - 2\beta/\alpha)} = \frac{0}{0} \tag{2.83}$$

By using the definition of the limit, it is clearly seen from equation (2.83) that L'Hospital Rule can be applied to calculate the $\Phi'(z_b)$ term. Applying L'Hospital Rule by taking the derivative of both the numerator and the denominator with respect to z of the limit defition of $\Phi'(z_b)$:

$$\Phi'(z_b) = \lim_{z \to z_b} \frac{\Phi(z) - \Phi(z_b)}{z - z_b} \tag{2.84}$$

$$\Phi'(z_b) = \lim_{z \to z_b} \frac{\Phi'(z) - 0}{1 - 0} = \lim_{z \to z_b} \Phi'(z) \tag{2.85}$$

$$\lim_{z \to z_b} \Phi'(z) = \frac{\alpha^2 - \alpha^2 z_b^2}{1 - z_b^2} - \frac{2z_b}{(1 + z_b - 2\beta/\alpha)} \tag{2.86}$$

$$\lim_{z \to z_b} \Phi'(z) = \frac{\alpha^2(1 - z_b^2)}{1 - z_b^2} - \frac{2z_b}{(1 + z_b - 2\beta/\alpha)} \tag{2.87}$$

By cancelling the $(1 - z_b^2)$ from the first term of equation (2.87), we obtain an expression for $\Phi'(z_b)$ finally as:

$$\Phi'(z_b) = \alpha^2 - \frac{2z_b}{(1 + z_b - 2\beta/\alpha)} \tag{2.88}$$

Similary, L'Hospital for $\Phi''(z_b)$;

$$\Phi''(z_b) = \lim_{z \to z_b} \frac{\Phi'(z) - \Phi'(z_b)}{z - z_b} = \lim_{z \to z_b} \Phi''(z) \tag{2.89}$$

By taking the derivative of equation (2.74), we obtain the equation for $\Phi''(z)$:

$$\Phi'' = \frac{-2\Phi\Phi'(1-z^2) + (\alpha^2 - \Phi^2)2z}{(1-z^2)^2} - \frac{-4z(1+z-2\beta/\alpha)}{(1+z-2\beta/\alpha)^2} \tag{2.90}$$

First term of equation (2.90) is indeterminate since the denominator and the nominator of it equals to zero. Then, by applying the L'Hospital Rule again:

$$\begin{aligned}\lim_{z\to z_b} \Phi''(z_b) = \\ \lim_{z\to z_b} \frac{-2[\Phi^2(1-z^2) + \Phi\Phi''(1-z) - 2z\Phi'] - 4z\Phi'\Phi + 2(\alpha^2-\Phi^2)}{2(1-z^2)(-2z)} \\ -\frac{-4z(1+z-2\beta/\alpha)}{(1+z-2\beta/\alpha)^2}\end{aligned} \tag{2.91}$$

By re-arranging the terms:

$$\lim_{z\to z_b} \Phi''(z_b) = \lim_{z\to z_b} \frac{-2\Phi'^2(1-z^2) - \Phi\Phi''(1-z^2) - 2\alpha^2(1-z^2)}{2(1-z^2)(-2z)} - A, \tag{2.92}$$

where $A = \frac{-4z(1+z-2\beta/\alpha)}{(1+z-2\beta/\alpha)^2}$.

Canceling the $(1-z^2)$ terms from the first term of RHS:

$$\Phi''(z_b) = \frac{-2\Phi'^2(z_b) - \Phi(z_b)\Phi''(z_b) + 2\alpha^2}{-4z_b} - \frac{2-4\beta/\alpha}{(1+z_b-2\beta/\alpha)^2} \tag{2.93}$$

Then, finally the equation (2.94) is obtained for $\Phi''(z_b)$ as shown below:

$$\Phi''(z_b) = \frac{(-2\Phi'^2(z_b) + 2\alpha^2)/(-4z_b) - (2-4\beta/\alpha)/(1+z_b-2\beta/\alpha)^2}{1-\Phi(z_b)/2z_b} \tag{2.94}$$

Similary, L'Hospital for $\Phi'''(z_b)$:

$$\Phi'''(z_b) = \lim_{z\to z_b} \frac{\Phi''(z) - \Phi''(z_b)}{z - z_b} = \lim_{z\to z_b} \Phi'''(z) \tag{2.95}$$

$$\lim_{z\to z_b} \Phi'''(z) = \lim_{z\to z_b} \frac{A}{(1-z^2)^4} + \frac{2-4\beta/\alpha}{(1+z_b-2\beta/\alpha)^4}, \tag{2.96}$$

where A is given by equation (2.97):

$$\begin{aligned}A = [-2\Phi'^2(1-z^2) - 2\Phi\Phi''(1-z^2) + 2(\alpha^2 - \Phi'^2)](1-z^2)^2 \\ -[-2\Phi\Phi'(1-z^2) + 2(\alpha^2-\Phi'^2)z](1-z^2)(-4z)\end{aligned} \tag{2.97}$$

The term $(1-z^2)$ can be cancelled from equation (2.96) and from the term A. Then we obtain:

$$\lim_{z\to z_b} \frac{(1-z^2)^2[-2\Phi'^2 - 2\Phi\Phi''] + (1-z^2)[2(\alpha^2-\Phi'^2) + 2\Phi\Phi'] + 8z^2(\alpha^2-\Phi'^2)}{(1-z^2)^3} + \frac{2-4\beta/\alpha}{(1+z_b-2\beta/\alpha)^4} = \lim_{z\to z_b} \Phi'''(z) \qquad (2.98)$$

By re-arranging terms;

$$\lim_{z\to z_b} \frac{-2\Phi'^2 - 2\Phi\Phi''}{1-z^2} + \lim_{z\to z_b} \frac{2(\alpha^2-\Phi'^2) + 2\Phi\Phi'}{(1-z^2)^2} + \lim_{z\to z_b} \frac{8z^2(\alpha^2-\Phi'^2}{(1-z^2)^3} + \lim_{z\to z_b} \frac{2-4\beta/\alpha}{(1+z_b-2\beta/\alpha)^4} = \lim_{z\to z_b} \Phi'''(z) \qquad (2.99)$$

Clearly seen from equation (2.99) that applying L'Hospital Rule to $\Phi'''(z_b)$ term needs very complicated process. Therefore, it is checked wheter derivation of $\Phi'''(z_b)$ term is practical or not by checking the order of the terms. When we look at the numerical values $\Phi''(z_b)$ attains, it is seen that order of $\Phi''(z_b)$ is about 10^{-4}. Compared to the third term of equation (2.81), the last term of the Taylor series expansion which involves $\Phi'''(z_b)$, at most attains an order of 10^{-7}. Because it is very difficult to obtain an analytical expression for $\Phi'''(z_b)$ and it has neglible effect on the calculation of $\Phi(z)$ -even no effect for the calculation of the eigenvalues-, this term is omitted from Taylor series expansion which was accumulated by Michalke [18]. Then our expression for $\Phi(z)$ becomes;

$$\Phi(z) = \Phi(z_b) + \Phi'(z_b)(z-z_b) + \frac{\Phi''(z_b)}{2!}(z-z_b)^2 \qquad (2.100)$$

After the calculation of the boundaries, normal RK4 procedure is applied as mentioned above. For temporal amplification approach, however there are some important changes to consider. The first change is in the Ricatti equation. In equation (2.54), instead of β/α variable, imaginary part of phase velocity c_i is used, due to temporal amplifications. The second change is RK4 integration, which is evaluated only in one direction, because of the fact that $\Phi_r(z)$ is an antisymmetric function and $\Phi_i(z)$ is a symmetric one. Therefore, 1-D simplex method becomes suitable for minimizing Φ at $z = 0$. The Ricatti Equation for the temporal approach transformed by the new

variable $z = tanhy$ is given below. It is time to remind that the disturbance wave number for the temporal approach is real (i.e. α is real).

$$\frac{d\Phi}{dz} = \frac{\alpha^2 - \Phi^2}{1 - z^2} - \frac{2z}{(1 + z - i2c_i)} \tag{2.101}$$

By using this equation and aplying the procedure with the changes of temporal approach, the eigenvalues are calculated for the temporal amplification case.

2.2 Runge-Kutta-Gill Method

Runge-Kutta is a common method to solve differential equations numerically. They are an important family of iterative methods for the approximation of solutions of the ordinary differential equations developed by C. Runge and M.W. Kutta.

Consider an initial value problem defined as;

$$\frac{d\mathbf{x}}{dt} = f(t, \mathbf{x}(t)) \tag{2.102}$$

Where $x(t) = (x1(t), x2(t), ...xn(t))^T$ and the function f is defined in the interval of $[a, b]$ real set of numbers with an initial condition;

$$\mathbf{x}(0) = \mathbf{x}_0 \tag{2.103}$$

To calculate numerically the solution of $x(t)$ over the interval $t \in [a, b]$, the interval $[a, b]$ is divided into the M equal subintervals. The ending points of this subintervals (i.e. the mesh points) can be defined as t_j. Then;

$$t_j = a + jh \tag{2.104}$$

Where $j = 0, 1, 2, ..., M$ and $h = (b - a)/M$. The term h is called as step size. The family of explicit Runge-Kutta (RK) methods of m'th stage can be stated as below;

$$\mathbf{x}(t_{n+1}) = \mathbf{x}_{n+1} = \mathbf{x}_n + h \sum_{i=1}^{m} c_i k_i \tag{2.105}$$

Where k defined as;

$$\begin{aligned}
&k_1 = f(t_n, x_n),\\
&k_2 = f(t_n + \alpha_2 h, \mathbf{x}_n + h\beta_{21} k_1(t_n, \mathbf{x}_n)),\\
&k_3 = f(t_n + \alpha_3 h, \mathbf{x}_n + h(\beta_{31} k_1(t_n, \mathbf{x}_n) + \beta_{32} k_2(t_n, \mathbf{x}_n))),\\
&.\\
&.\\
&k_m = f(t_n + \alpha_m h, \mathbf{x}_n + h \sum_{j=1}^{m-1} \beta_{mj} k_j)
\end{aligned} \tag{2.106}$$

Specific Runge-Kutta methods can be defined by providing particular m (the number of stages), and the coefficients α_i (for i = 2,3,..,m), β_{ij} (for 1$\leq j < i \leq m$), and c_i (for i = 1,2,..,m).

A fourth order Runge-Kutta (RK4) method can be defined by setting $m = 4$. For Gill's method for a fourth order Runge-Kutta, the formula should be as below with specific α and β values;

$$x_{n+1} = x_n + \frac{1}{6}[k_1 + (2 - \sqrt{2})k_2 + (2 + \sqrt{2})k_3 + k_4] + O(h^5) \tag{2.107}$$

Where k_n values are defined as;

$$\begin{aligned}
k_1 &= hf(t_n, x_n)\\
k_2 &= hf(t_n + \frac{1}{2}h, x_n + \frac{1}{2}k_1)\\
k_3 &= hf(t_n + \frac{1}{2}h, x_n + \frac{1}{2}(-1 + \sqrt{2})k_1) + (1 - \frac{1}{2}\sqrt{2})k_2\\
k_4 &= hf(t_n + h, x_n - \frac{1}{2}\sqrt{2}k_2 + (1 + \frac{1}{2}\sqrt{2})k_3
\end{aligned} \tag{2.108}$$

2.3 Downhill Simplex Algorithm

The downhill simplex method was proposed by Nelder and Mead. Only function evaluations is enough for the method, the derivatives of the functions are not needed. Therefore, it is not a very efficient method in terms of the number of function evaluations that it requires. The downhill simplex method may frequently be the best

method to use, if the aim is “get something working quickly” for a problem whose computational burden is small [22].

The method has a geometrical naturalness by which description of the method can be understood easily. A simplex is the geometrical figure consisting of N dimensions and of $N + 1$ points (or vertices) and all their interconnecting line segments, polygonal faces, etc. For two-dimensional case, simplex becomes triangle. In three dimensionals, it is a tetrahedron, not necessarily the regular tetrahedron.

In one-dimensional minimization process, it is possible to restrict a minimum, so that the success of a subsequent isolation is guaranteed. For multidimensional cases; however, the best thing to do is to assign a starting guess to the algorithm which is a vector of independent variables as the first point to try. Then, the algorithm is supposed to make its own way downhill through the unimaginable complexity of an N-dimensional topography, until it encounters a (local, at least) minimum.

Therefore, the downhill simplex method must be started not just with a single point, but with $N + 1$ points which defines an initial simplex. If there is only one point of initial starting points $\mathbf{P}_0$, then the other N points can be defined by the equation below.

$$\mathbf{P}_i = \mathbf{P}_0 + \lambda \mathbf{e}_i \tag{2.109}$$

In the equation above, the $\mathbf{e}_i$’s are N unit vectors, and where λ is a constant which is the problem’s characteristic length scale (different λ_i’s can be defined for each vector direction, also).

The downhill simplex method takes a series of steps, most steps are just moving the point of the simplex, which has the largest value of the function (“highest point”) through the opposite face of the simplex to a lower point. These movement is called as "reflection", and it is constructed to conserve the volume of the simplex (hence maintain its non degeneracy).

The method can also expand the simplex in one or another direction to take larger steps and when it reaches a “valley floor,” the method can contract itself in the trans-

verse direction and tries to ooze down the valley.

If there is a situation where the simplex is trying to “pass through the eye of a needle,” it contracts itself in all directions, pulling itself in around its lowest (best) point. The basic moves of the method are summarized in Figure 2.2.

In Figure 2.2, a tetrahedron is shown at the top. It is the beginning sets of points for the downhill simplex method. The simplex at the end of the step can be any one of (a) a reflection away from the high point, (b) a reflection and expansion away from the high point, (c) a contraction along one dimension from the high point, or (d) a contraction along all dimensions towards the low point. By using appropriate sequence of such steps the method converges to a minimum of the function.

Termination criteria can be delicate in any multidimensional minimization routine. It may not be possible to have the option of requiring a certain tolerance for a single independent variable without bracketing for multiple independent variables (i.e. multidimensional simplex method). In these situations, "cycle" or "step" can be defined to terminate the vector distance moved in that step that is fractionally smaller in magnitude than some tolerance tol. Alternatively, the algorithm can be designed to terminate, when the decrease in the function value in the terminating step be fractionally smaller than some tolerance $ftol$.

2.4 Post-Processing Algorithms

By calculating the eigenvalues of the transformed Ricatti Equation (equation (74)), behaviour of the disturbances in the shear layer can be understood, i.e. the value of β corresponding to the most strong amplification rate can be determined, etc. However, to interpret and examine the instability mechanism in detail, the eigenvalues and the related eigenfunctions are not enough.

The flow patterns observed in the experiments are physically quantifiable (i.e. streaklines can be observed by implementing dye or smoke to the flows). Therefore, to compare the results of the analytical methods with the experimental ones, the visual-

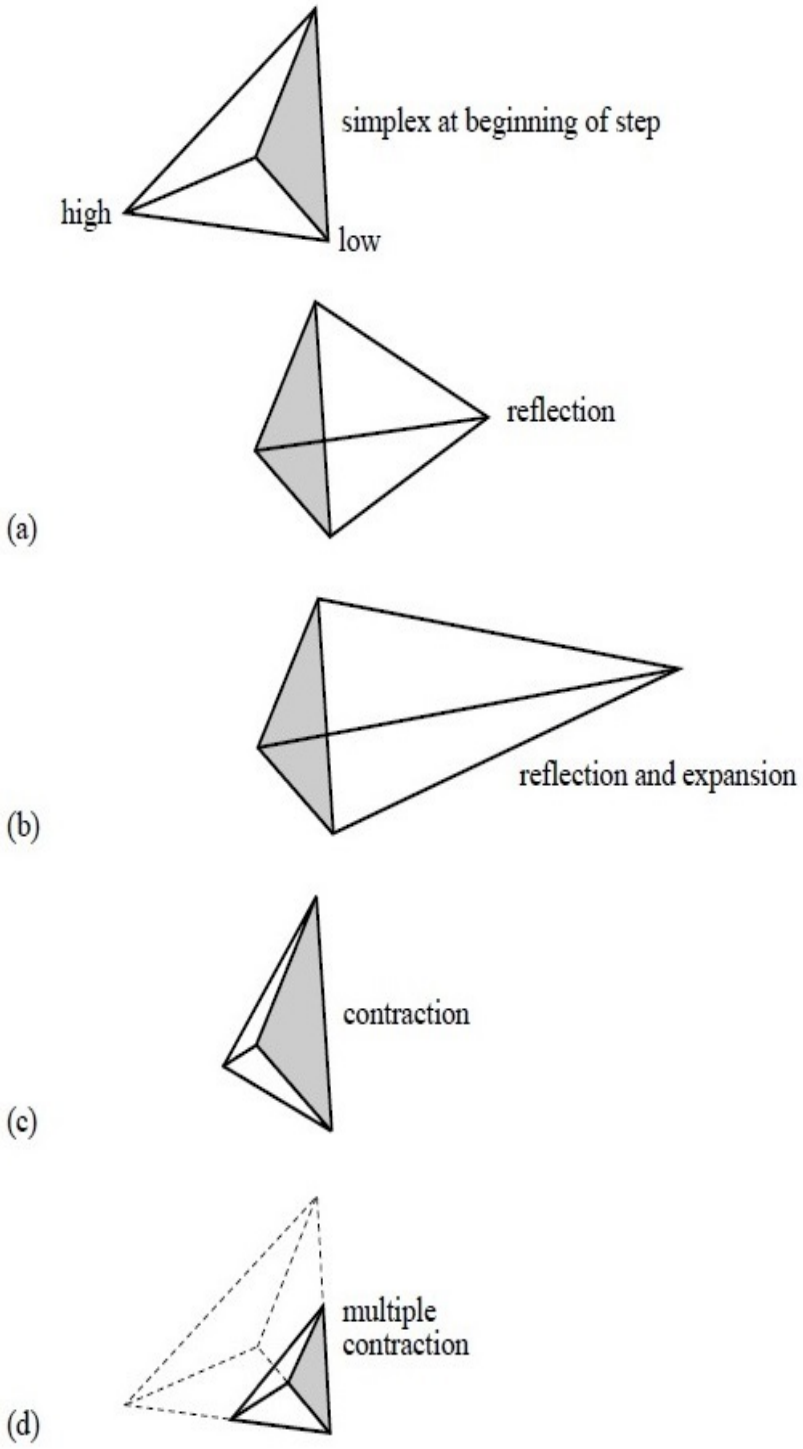

Figure 2.2: Different step types in the downhill simplex method

ization of the flow is another beneficial tool.

To calculate the vorticity amplitudes, the vorticity distributions and to visualize the flow, additional algorithms are needed in addition to the Fortran code used to calculate the eigenvalues.

First, the vorticity amplitudes and the vorticity distribution of the flow can be calculated by using the eigenvalues and the corresponding eigenfunctions of the Ricatti Equation. To calculate the vorticiy amplitudes ω, by re-arranging the terms of equation (2.23), an expression for ω term is obtained. The reason why equation (2.23) is used instead of the equation (2.27) is that equation (2.23) only depends on the eigenfunctions ϕ. To calculate ω with equation (2.23), the second derivative of the eigenfunctions ϕ'' is also needed.

$$\omega(y) = -\{U''/(U - \beta/\alpha)\}\phi \tag{2.110}$$

By putting U' term given by equation (2.65) into equation (2.5), which defines Ω_0, and calculating Ω_1 with equation (2.17), the total vorticity distribution of the flow can be obtained by equation (2.8). Ω_0 is then;

$$\Omega_0 = -U' = -0.5sech^2(y) \tag{2.111}$$

And Ω_1;

$$\Omega_1 = R\{\omega(y)e^{i(\alpha x - \beta t)}\} = e^{-\alpha_i x}\{\omega_r(y)cos(\alpha_r x - \beta t) - \omega_i(y)sin(\alpha_r x - \beta t)\} \tag{2.112}$$

Sum of the total vorticity of the basic flow and the disturbances;

$$\begin{aligned} &\Omega(x, y, t) = -0.5sech^2 y + \epsilon e^{-\alpha_i x} A \\ &A = \{\omega_r(y)cos(\alpha_r x - \beta t) - \omega_i(y)sin(\alpha_r x - \beta t)\} \end{aligned} \tag{2.113}$$

Using equation (2.113) in sweeping different x and y values, constant vorticity lines of the shear flow can be obtained.

Secondly, the pathlines and the streaklines are obtained by using velocity fields given

by equations (2.6) and (2.7). The velocity components of the disturbances are obtained with using the stream functions (equations (2.14) and (2.15)).

$$u_1 = \frac{\partial \psi_1}{\partial y} = \frac{\partial R\{\phi(y)e^{i(\alpha x - \beta t)}\}}{\partial y} \tag{2.114}$$

$$\frac{\partial R\{\phi(y)e^{i(\alpha x - \beta t)}\}}{\partial y} = e^{-\alpha_i x}\{\phi_r'(y)cos(\alpha_r x - \beta t) - \phi_i'(y)sin(\alpha_r x - \beta t)\} = A \tag{2.115}$$

Then, sum of the velocity of the main flow in x-direction with the disturbance velocity component u_1 yields;

$$u(x, y, t) = 0.5[1 + tanhy] + \epsilon e^{-\alpha_i x} A \tag{2.116}$$

For y-component of the velocity field, only the disturbance velocity is considered.

$$v = v_1 = -\frac{\partial \psi_1}{\partial x} = -\frac{\partial R\{\phi(y)e^{i(\alpha x - \beta t)}\}}{\partial x} \tag{2.117}$$

$$\begin{aligned} v(x, y, t) = \epsilon e^{-\alpha_i x}\{&[\alpha_i \phi_r(y) + \alpha_r \phi_i(y)]cos(\alpha_r x - \beta t) \\ &+ [\alpha_r \phi_r(y) + \alpha_i \phi_i(y)]sin(\alpha_r x - \beta t)\} \end{aligned} \tag{2.118}$$

The velocity components define the motion of a particle as shown below:

$$\frac{dx}{dt} = u(x(t), y(t), t) \qquad \frac{dy}{dt} = v(x(t), y(t), t) \tag{2.119}$$

Where right-hand sides of the equation (2.119) has already been obtained. Integrating the equation, the motion of a particle can be simulated. The functions $x(t)$ and $y(t)$ are position functions of the particles at a given time t. In order to define a specific pathline different initial conditions and time values can be used. The initial positions of the particles are defined by equation (2.120).

$$x(t_0) = x_0 \qquad y(t_0) = y_0 \tag{2.120}$$

Pathlines of the particles are calculated for different initial time values to simulate the release of the particles of the flow at different times from fixed locations. By connecting the end points of these pathlines, streaklines patterns are drawn.

CHAPTER 3

VALIDATION OF THE FORTRAN CODE & FURTHER DISCUSSION

3.1 Eigenvalues & Eigenfunctions

By using the algorithms described in the previous sections, eigenvalues of the Ricatti Equation given by equation (2.54) in Section 2.1 are obtained for different disturbance frequencies. For the spatial growth of the disturbances, the real and imaginary parts of the eigenvalues are given in Table 3.1.

To validate the results of the code, the eigenvalues for more frequent β values are plotted with the ones calculated by Michalke [18]. In Figures 3.1 and 3.2, red diamonds indicate the real and imaginary parts of the eigenvalues calculated by Michalke and the continuous blue lines show the results of the Fortran code developed.

In Figures 3.1 and 3.2, it is clearly seen that the results of the Fortran code developed in-house and the calculations of the Michalke are in perfect agreement. Since the spatial amplification rates are characterized by the imaginary parts of the eigenvalues, it is more important to investigate the α_i values in Figure 3.2.

When Figure 3.2 is examined, it will be seen that $-\alpha_i$ reaches to a maximum at a specific β value around 0.2, meaning that the growth rate of the disturbances becomes highest. To be specific, at $\beta = 0.2067$, the disturbance growth rate becomes maximum with $\alpha_i = 0.2284$. The value of α_r is 0.4031 at this specific β.

For the temporal growth of the disturbances, the eigenvalues calculated are the imaginary parts of the complex phase velocity c and α has no imaginary part. Disturbance growth rates are characterized by the product of c_i and α.

Table 3.1: Eigenvalues of the spatial disturbance growth case

β	α_r	α_i	c
0.5	1	0	0,5
0.45	0.925834	-0.04564	0.486048
0.4	0.844473	-0.091685	0.473668
0.35	0.753627	-0.137311	0.464421
0.3	0.649725	-0.180609	0.461734
0.25	0.52717	-0.216245	0.47423
0.2	0.381031	-0.227903	0.524892
0.15	0.234138	-0.187966	0.640649
0.1	0.129198	-0.11878	0.774006
0.05	0.056408	-0.054556	0.886399

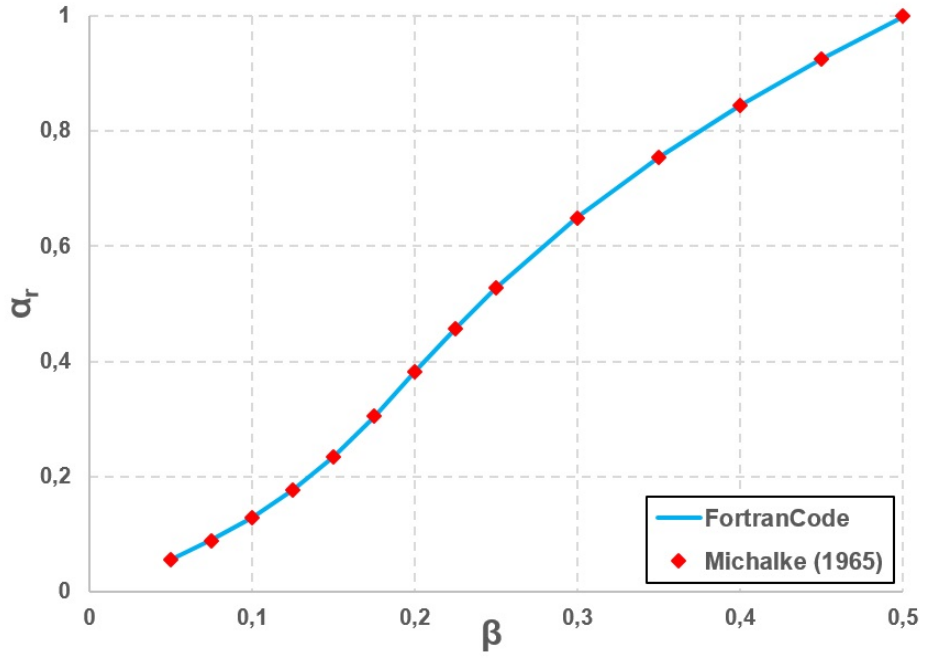

Figure 3.1: Real parts of eigenvalues calculated with spatial amplification theory.

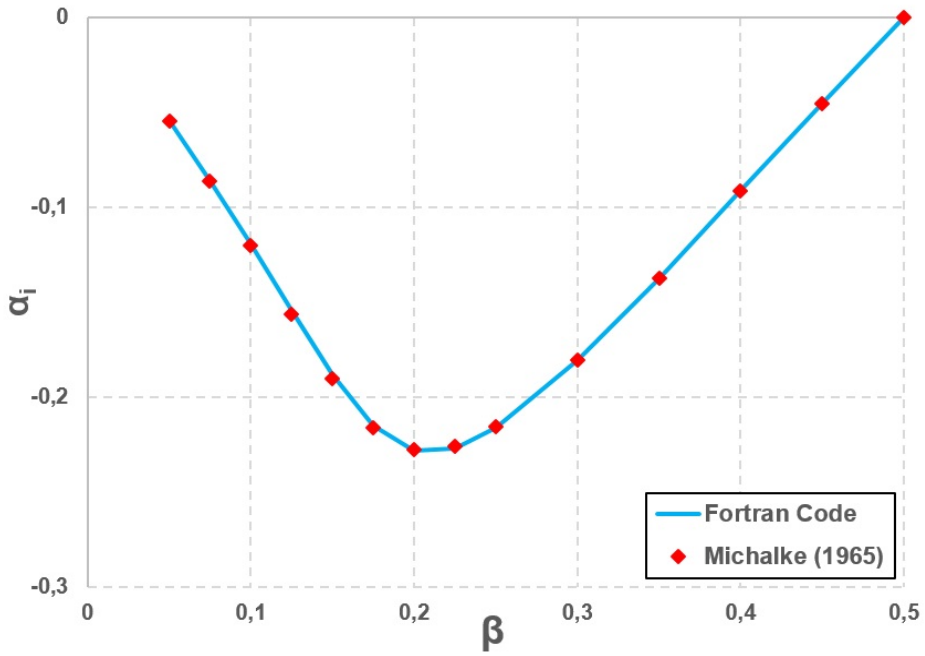

Figure 3.2: Imaginary parts of eigenvalues calculated with spatial amplification theory.

Calculations of the temporal disturbance growth are done for different wavenumbers instead of the different frequencies, since the disturbance frequencies do not directly appear in the Ricatti equation for temporal case (equation (2.101) in Section 2.1). The results are tabulated in Table 3.2.

To validate the results of the code for the temporal case, the disturbance growth rates obtained are compared with the calculations of Michalke [16]. In Figure 3.3, red diamonds indicate the temporal growth rates calculated by Michalke and the continuous black line shows the results of the Fortran code developed.

With the results shown in Figure 3.3, it is understood that the algorithm of the code is capable of calculating the temporal amplifications of the disturbances correctly.

When Figure 3.3 is examined, it is seen that the temporal amplification rate becomes maximum at a specific α value around 0.2, just like the case for the spatial theory. The growth rate gets its highest value as 0.0949 at $\alpha = 0.4446$.

Table 3.2: Eigenvalues of the temporal disturbance growth case

α	c_i	αc_i
1	0	0
0.9	0.032383	0.0291447
0.8	0.066843	0.0534744
0.7	0.103613	0.0725291
0.6	0.143281	0.0859686
0.5	0.186602	0.093301
0.4	0.234922	0.0939688
0.3	0.290747	0.0872241
0.2	0.360156	0.0720312
0.1	0.468555	0.0468555
0	0.5	0

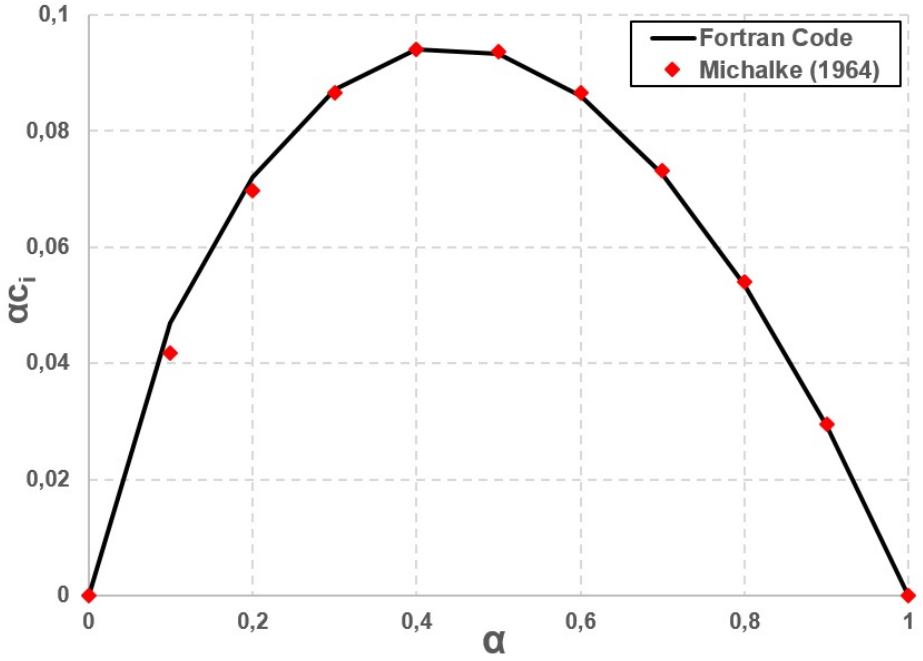

Figure 3.3: Disturbance growth rates calculated with temporal amplification theory.

To check whether the results of the temporal theory are consistent with the ones calculated by spatial theory, the amplification rates of the both theories are plotted as shown in Figure 3.4. For temporal disturbance growth, the disturbance frequencies are obtained by using its relation with the phase velocity, $\beta_r = c_r \alpha_r$.

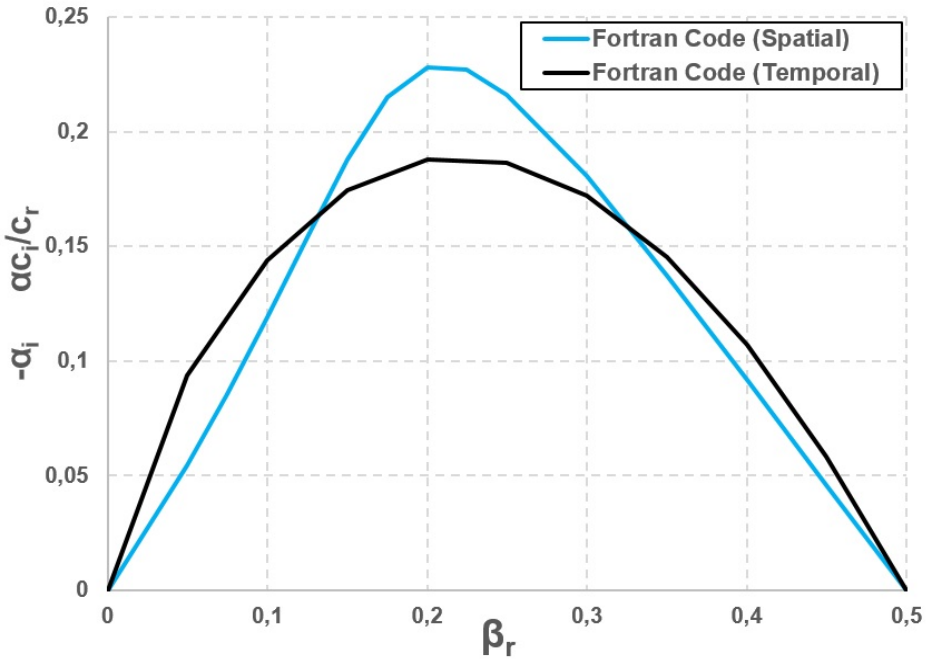

Figure 3.4: Comparison of amplification rates calculated with spatial and temporal amplification theories.

It is observed from Figure 3.4 that the temporal and spatial amplification theories have same trend for the amplification rates; they get maxima for specific disturbance frequencies as the frequency increases. After the maxima, the amplification rates damp with the increasing frequency values. For small disturbance frequencies the difference between the disturbance growth rates of the temporal and the spatial amplification theory is higher compared to larger disturbance frequencies.

The higher differences at the amplification rates for the lower values of β_r pose an important question. Which theory is more convenient to predict the instability characteristics correctly? Therefore, it was needed to check the results of the Fortran code for two approaches with experimental data. In Figure 3.5, the amplification rates

obtained by the code for temporal and spatial approaches are plotted with the experimental results of Freymuth [17]. Freymuth [17] used an axissymetric jet (shown with yellow circles in Figure 3.5) and a plane jet (shown with green squares in Figure 3.5) while conducting his experiments. Freymuth [17] used scale factor while plotting the amplification rates with respect to the Strouhal number -defined as $f\theta/U_0$ (Where f was the frequency of sound to produce disturbance, θ was momentum thickness and U_0 was jet velocity). Velocities of axis-symmetric and plane jets were 8 m/s in the experiments. Because Rayleigh equation was derived from two-dimensional Helmholtz vorticity equation, both the results of experiments of plane and axissymmetric jets may be used to validate the theories, since both geometries have the same cross section in 2-D.

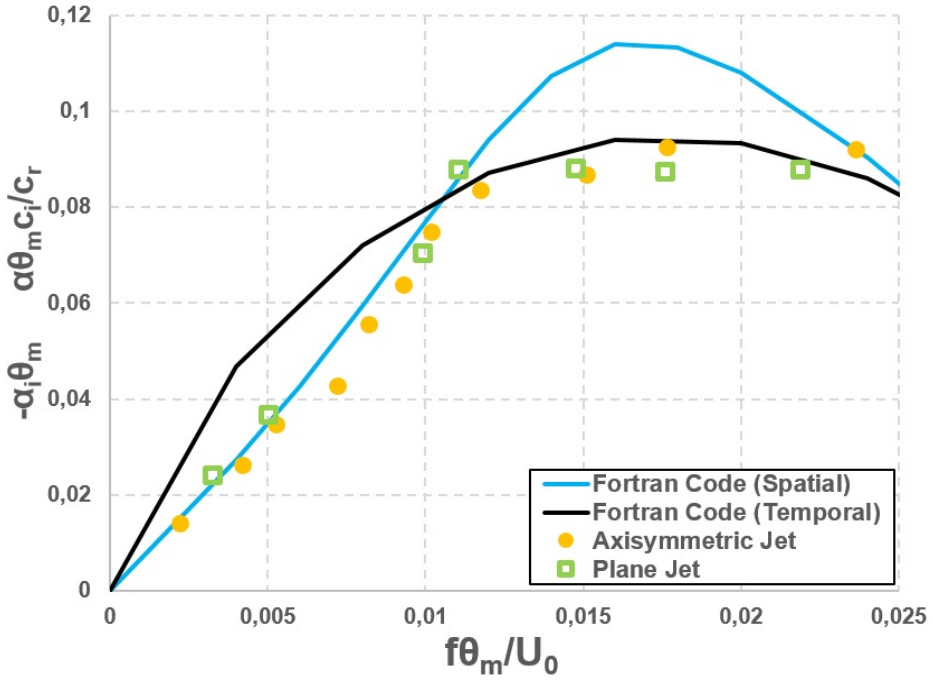

Figure 3.5: Comparison of the spatial and temporal theories with experimental results.

In Figure 3.5, the results of the experiments conducted by Freymuth [17] are almost overlapping the amplification rates of the spatial case for lower disturbance frequencies. Therefore, it can be said that the spatial approach reflects the characteristics of the disturbances with greater fidelity than the temporal approach at lower frequencies. As the disturbance frequencies increase, the temporal amplification values becomes

closer to the experimental ones. However, since the spatial theory involves some essential features of instability properties of the free boundary layers which will be explained while examining the derivatives of the eigenfunctions, the focus of this thesis is on the spatial amplifications.

Because the eigenfunctions appear in certain flow parameters (i.e. y-component of the disturbance velocity component, the vorticity amplitudes,...etc.), they have significant role while interpretting the instability mechanism. Therefore, first the eigenfunctions of the transformed Ricatti Equation are calculated and are compared with the results of Michalke [18] for the spatial case. From Figures 3.6, 3.7, 3.8 and 3.9, it can be seen that the Fortran code developed in-house gives very accurate results for the different disturbance frequencies.

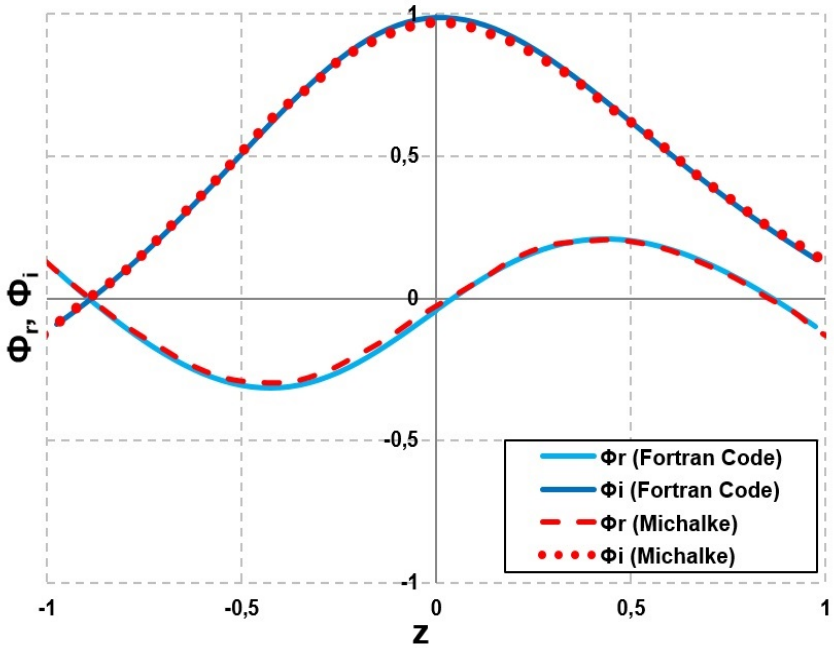

Figure 3.6: Real and imaginary parts of the eigenfunctions of transformed Ricatti equation for $\beta = 0.1$

To obtain eigenfunctions of Rayleigh Equation a reverse transformation from y to z is necessary. This is achieved by solving a system of differential equations involving the transformed Ricatti Equation and the equation for dz/dy. Therefore, integration should be done in two steps. The real and imaginary parts of the eigenfunctions

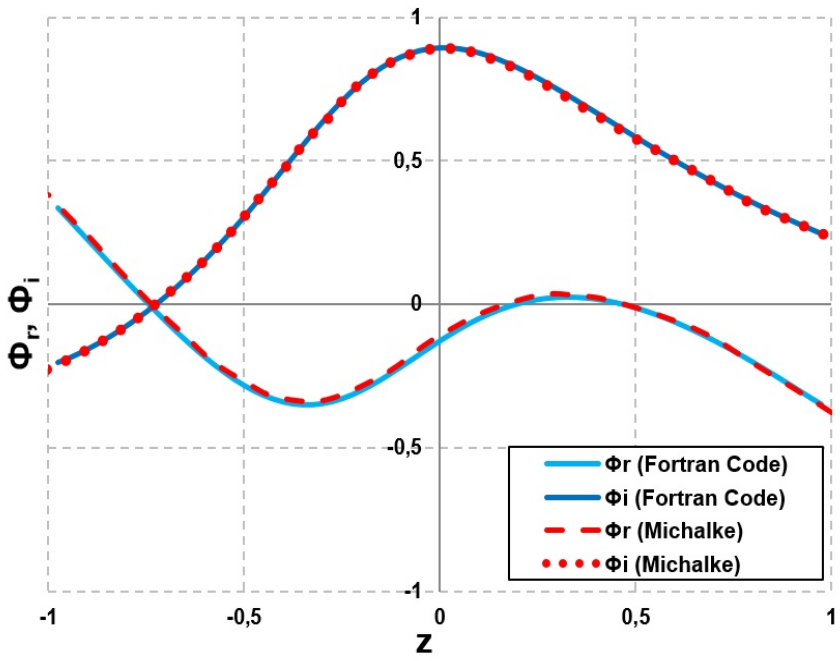

Figure 3.7: Real and imaginary parts of the eigenfunctions of transformed Ricatti equation for $\beta = 0.2$

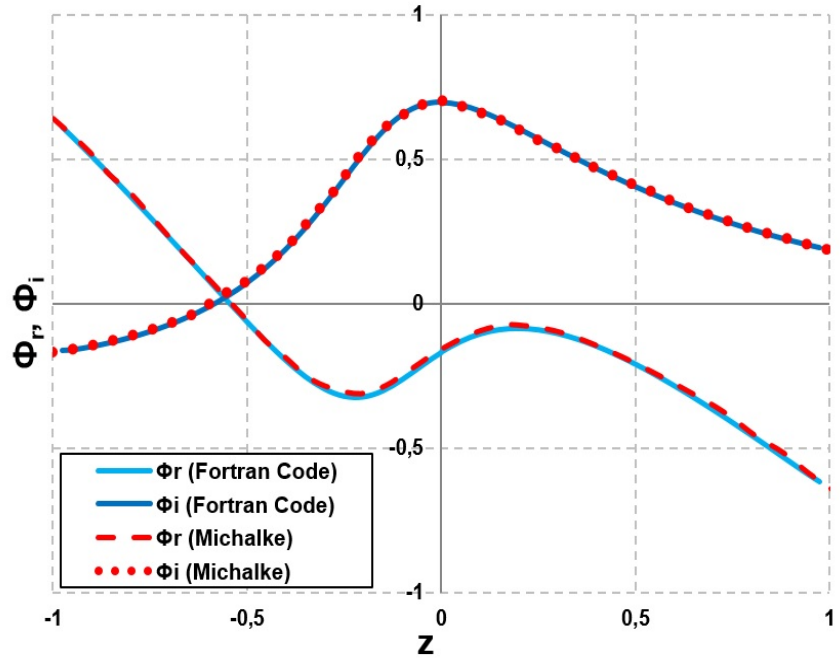

Figure 3.8: Real and imaginary parts of the eigenfunctions of transformed Ricatti equation for $\beta = 0.3$

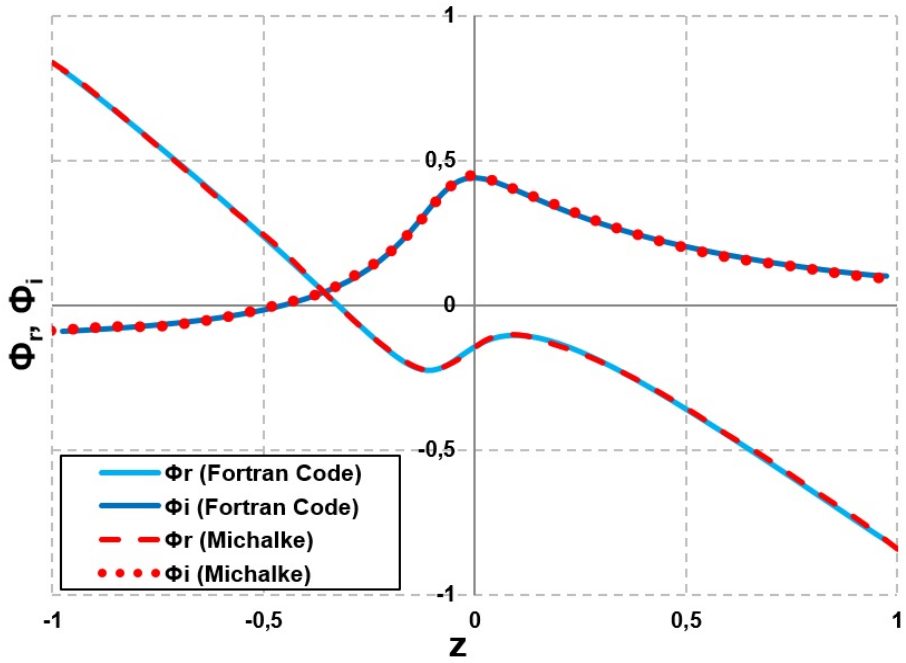

Figure 3.9: Real and imaginary parts of the eigenfunctions of transformed Ricatti equation for $\beta = 0.4$

obtained for different disturbance frequencies are shown in Figure 3.10 and 3.11, respectively.

In Figure 3.12, the eigenfunctions of Rayleigh Equation for the temporal and spatial cases can be seen at their most strongly amplifying frequencies. The real part of the eigenfunction of the temporal case shows a symmetric characteristic and the imaginary part has an antisymmetric function characteristic as mentioned in Section 2.1. This situation changes for the spatial theory, however. For the spatial theory, both the real and the imaginary parts of the eigenfunctions have no symmetric or antisymmetric features.

The derivatives of the eigenfunctions of Rayleigh Equation also have importance since they are related to x-component of the disturbance velocity u_1. Thus, they become useful while comparing the results of the theories with the experiments.

Michalke [18] stated that in the experiments, a phase reversal was observed outside

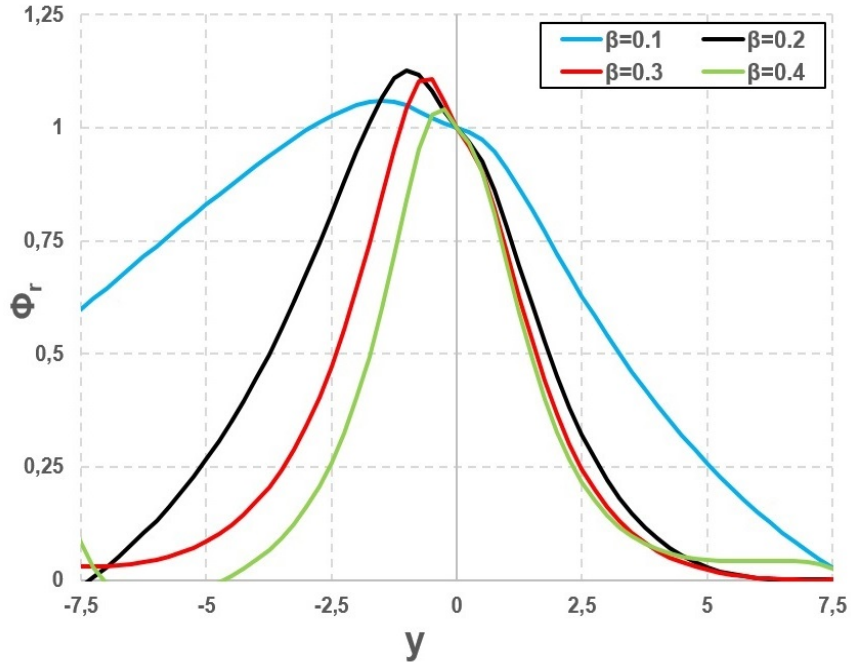

Figure 3.10: Real parts of the eigenfunctions of the Rayleigh Equation for the spatial theory.

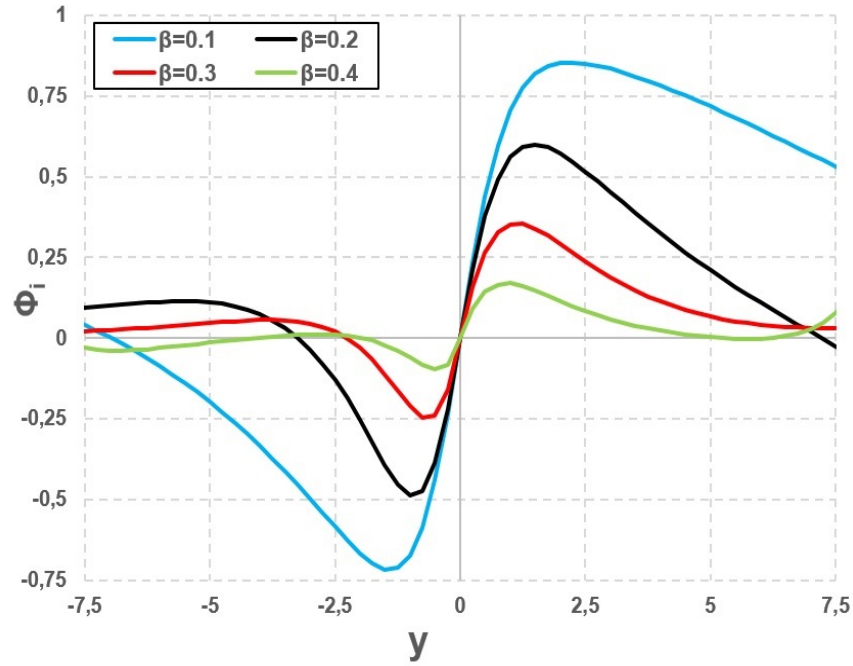

Figure 3.11: Imaginary parts of the eigenfunctions of the Rayleigh Equation for the spatial theory.

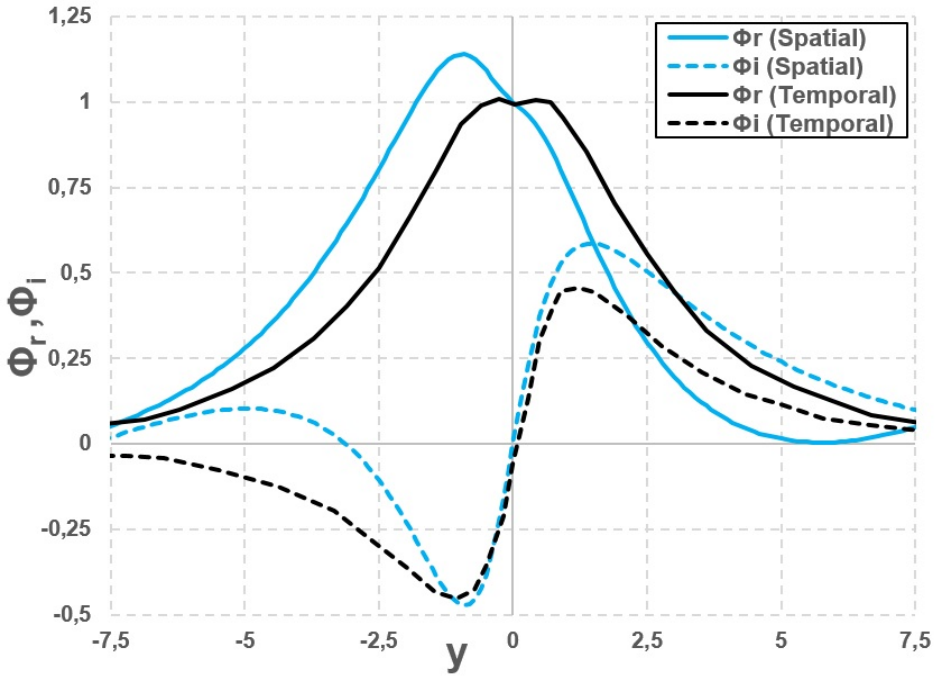

Figure 3.12: Comparison of the spatial and temporal theories at their maximum disturbance growth frequencies.

of the critical layer. Phase reversal means that the velocity component in the flow direction becomes zero.

For spatial theory, the real and the imaginary parts of the eigenfunctions become zero at almost the same values of y, shown in Figures 3.13 and 3.14. Therefore, a phase reversal condition is obtained at the negative values of y by the spatial approach.

On the other hand, the temporal theory has symmetric and antisymmetric trends for the real and imaginary parts of the eigenfunction derivatives, meaning that ϕ_r, ϕ_i become zero at different values of y. This results in the absence of the phase reversal in temporal approach while it occurs in experiments.

Then, it is not wrong to state that the spatial approach is more useful than the temporal one to investigate the free boundary layers. In physical point of view, this situation also makes sense since the disturbances observed in the experiments grow in space not in time.

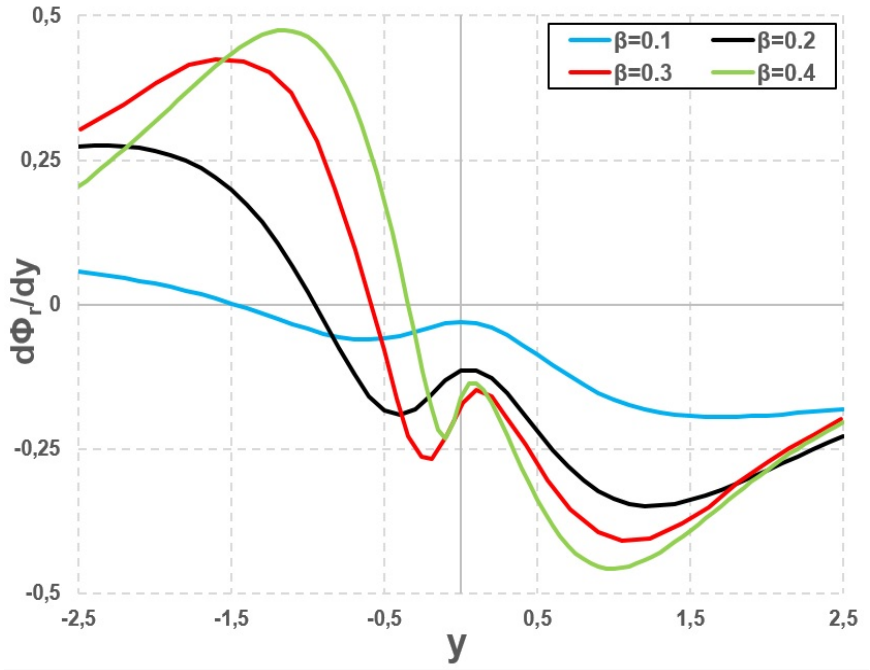

Figure 3.13: Real parts of derivatives of eigenfunctions at various frequencies for the spatial theory.

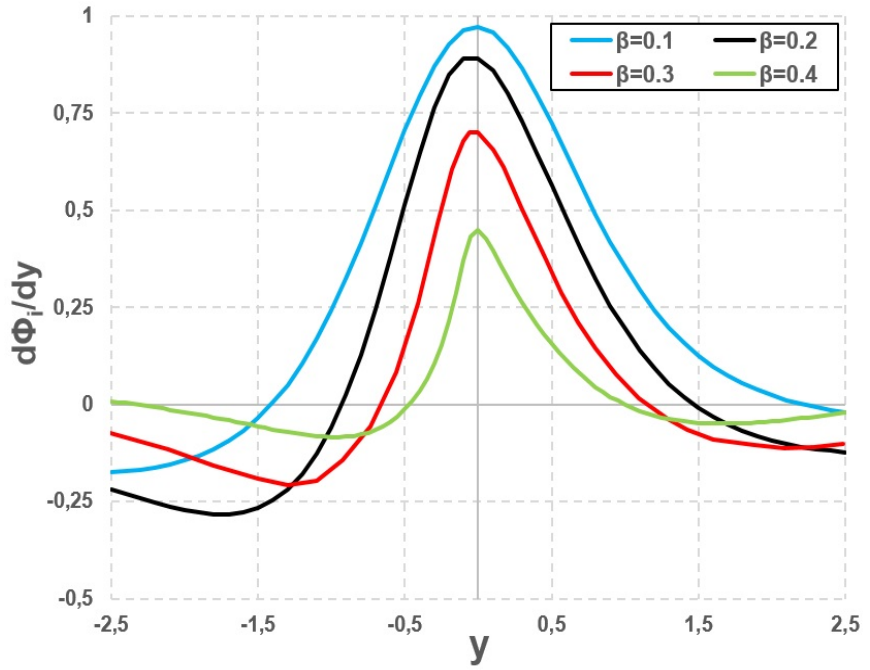

Figure 3.14: Imaginary parts of derivatives of eigenfunctions at various frequencies for the spatial theory.

3.2 Vorticity Amplitudes & Total Vorticity Distribution

Eigenvalues and eigenfunctions are not enough to examine the shear layer on their own. The vorticity distribution of the disturbed flow helps more to understand the instability mechanism. First step to calculate the vorticity distribution is the calculation of the vorticity amplitudes.

From Figures 3.15, 3.16, 3.17 and 3.18, vorticity amplitudes calculated by the Fortran code and the results of Michalke [18] are compared for different disturbance frequencies. Obviously, the vorticity amplitudes of the Fortran code are totally compatible with the literature data.

When the figures are examined, it will be seen that the vorticity amplitudes increase with the increasing disturbance frequency, as expected. It is also notable that for the negative values of y, meaning that the lower region of the shear layer, the vorticity amplitudes get higher values.

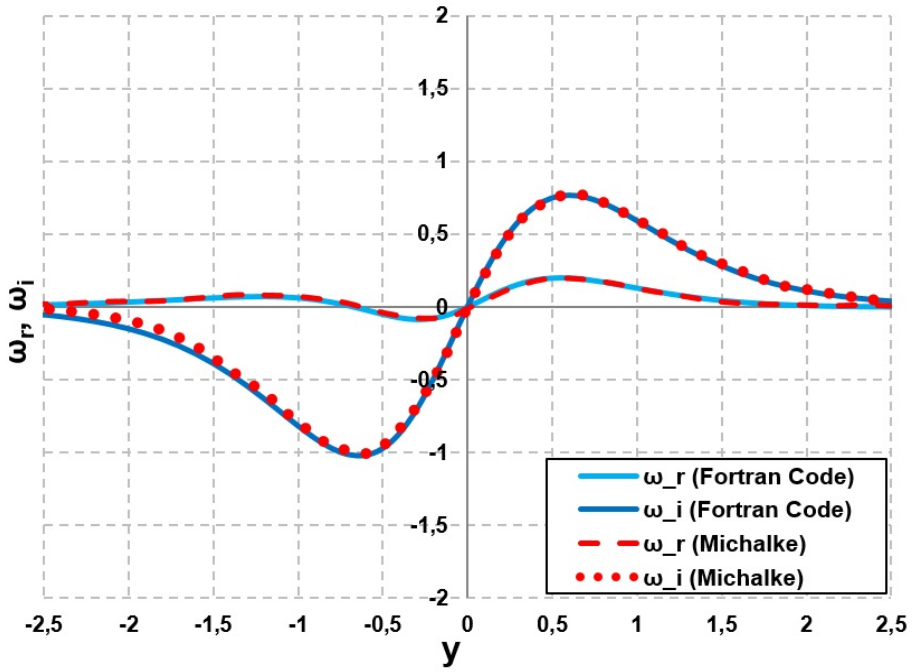

Figure 3.15: Vorticity amplitudes for $\beta = 0.1$.

After the validation of the vorticity amplitudes, the vorticity distribution of the shear

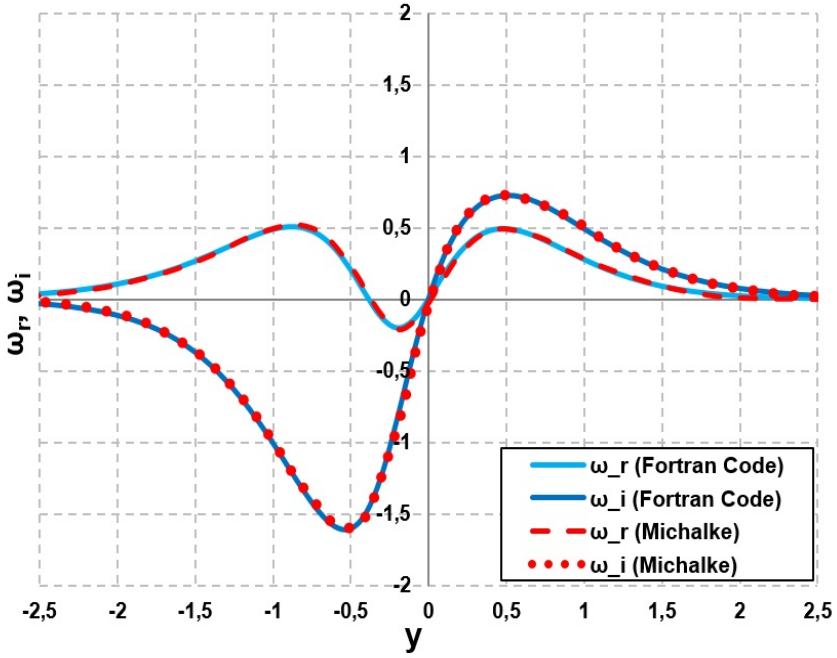

Figure 3.16: Vorticity amplitudes for $\beta = 0.2$.

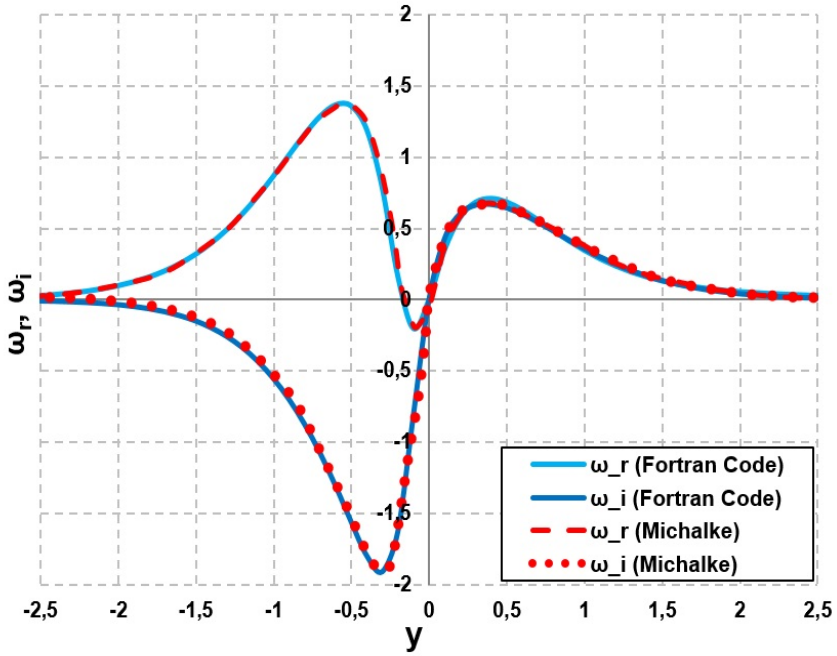

Figure 3.17: Vorticity amplitudes for $\beta = 0.3$.

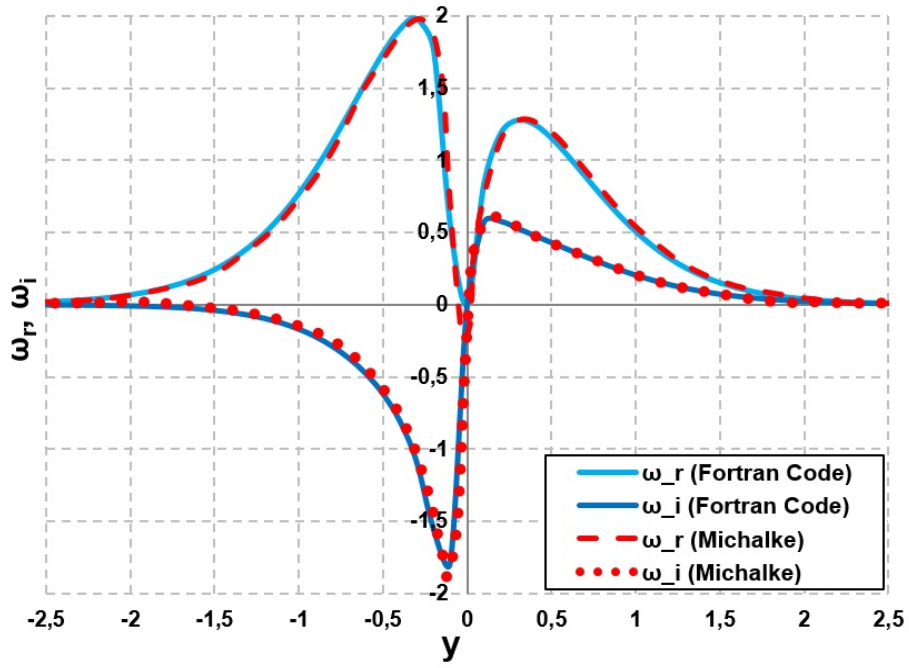

Figure 3.18: Vorticity amplitudes for $\beta = 0.4$.

flow were calculated by using equation (2.113) in Section 2.4. Constant vorticity lines are plotted along twice of the disturbance wavelength λ at two different times $(t = T, t = 1 : 5T)$. The disturbance wavelength equals to $2\pi/\alpha_r$. For most strongly amplifying disturbances $\alpha_r = 0.4031$, which yields $\lambda = 15.587$.

Time value T is equal to $2\pi/\beta$ which is calculated as 30.398s for the most strongly amplified disturbance frequency $\beta = 0.2067$. The disturbance magnitude was chosen as $\epsilon = 0.0005$. The magnitude of the local disturbance equals to $\epsilon e^{-\alpha_i x}$ increasing along the wavelength.

The vorticity distributions at two different times can be seen in Figures 3.19 and 3.20. In these figures, the constant vorticity lines are straight at the beginning and by increasing local disturbance, they are distributed. Two peaks of vorticity are observed - one is for $y > 0$ and the other is for $y < 0$. The vorticity peak in lower region is bigger than the one in upper region at $t = T$. This is an expected result since the vorticity amplitudes at the lower region have higher values. Mutual induction of these peaks of the vorticity with time causes a rotational motion on the flow.

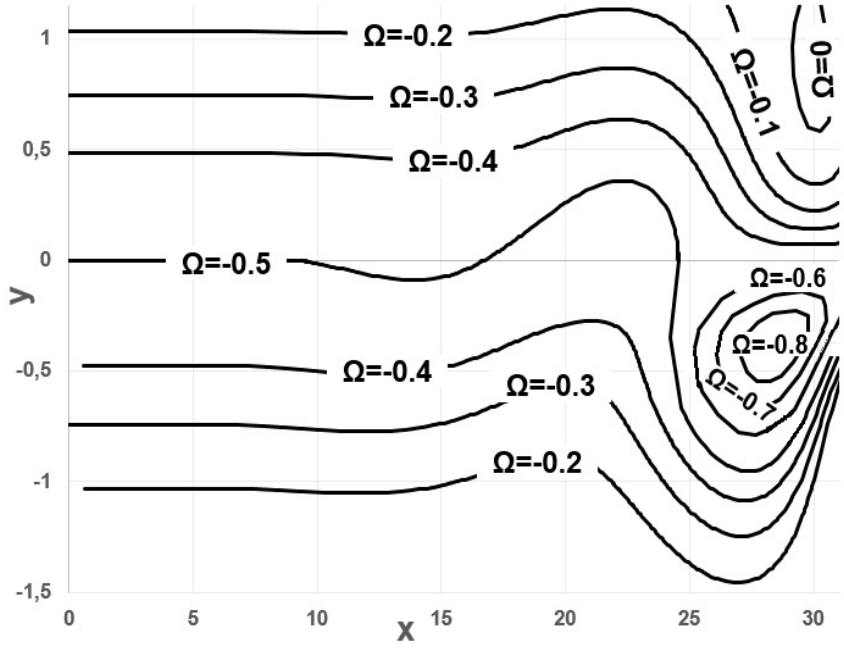

Figure 3.19: Constant vorticity lines at $t = T$, disturbance magnitude $\epsilon = 0.0005$

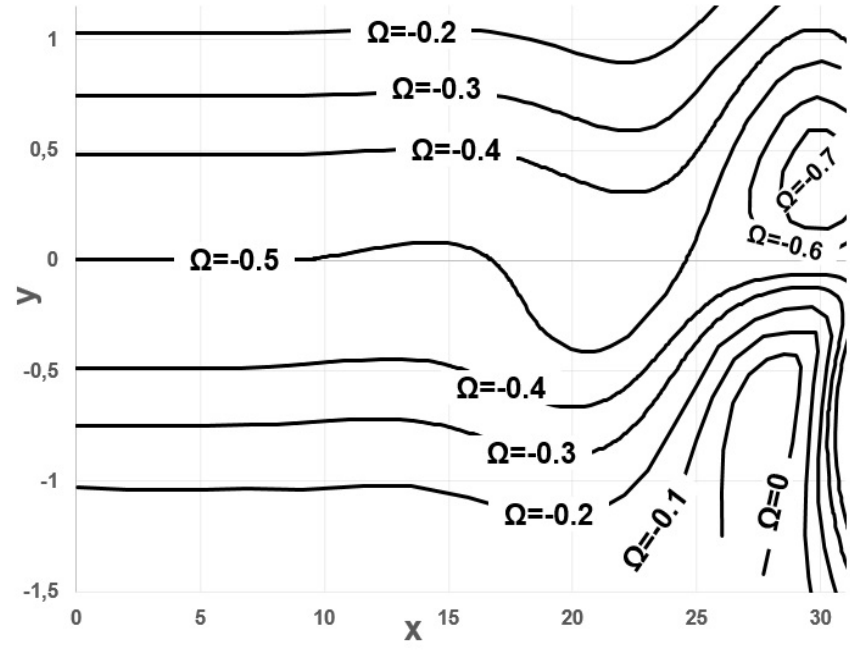

Figure 3.20: Constant vorticity lines at $t = 1.5T$, disturbance magnitude $\epsilon = 0.0005$

3.3 Pathlines & Streaklines

Investigation of the pathlines and the streaklines of the shear flow is very beneficial since they help to monitor the flow. It also provides an opportunity to compare the results obtained by the theory with the experiments visually. Streakline patterns are more useful than the pathlines due to its spatial formation just like the growth of the disturbances. Moreover, the experiments performed by injecting dye or smoke to the flow reflects the streaklines patterns.

To calculate the streaklines of the flow, there are two steps just like the calculation of the total vorticity distribution described in the previous section. First, the pathlines are calculated by using velocity distribution of the disturbed flow. The velocity distribution is calculated using the relation between the streamlines and the velocities as mentioned in Section 2.4.

Motion of a particle released into the flow at time t_0 can be simulated by equation (2.119) in Section2.4. The initial locations of the particles are chosen at $x_0 = 0$ and $y_0 = 0, \pm 0.48, \pm 1.03$. The y_0 values are determined by the help of the vorticity distributions calculated in the previous section. In Figures 3.19 and 3.20, at the locations next to the y_0 values mentioned, the constant vorticity lines with the basic total vorticity $\omega_0 = -0.5, -0.4, -0.2$ can be seen.

In Figure 3.21, the pathlines of the particles released at $t_0 = 0$ from different y_0 locations are shown. The motion of the particles are stopped at $t = T$ where T is the period equal to $2\pi/\beta$, since the disturbance flow is periodic. For this figure and the following figures of pathlines and streaklines, β is chosen as 0.2067 at which the disturbances grow most strongly and T equals to $30.4s$. The disturbance magnitude was chosen as $\epsilon = 0.0005$ again to correctly correlate the results with the total vorticity distributions obtained in the previous section. Clearly seen from Figure 3.21, the length of the paths decrease when the particle are released from lower region of shear layer for a constant time period. This is an expected result due to the hyperbolic tangent velocity profile. As the y value decreases for the velocity profile, the basic flow velocity U becomes slower.

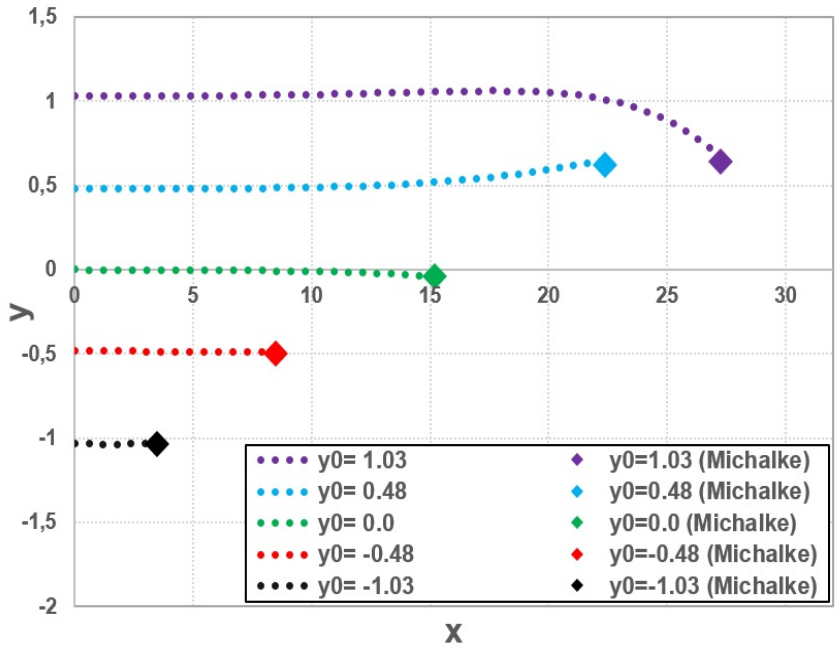

Figure 3.21: Pathlines calculated by the code and the particle locations of Michalke.

The diamonds at the end of the pathlines shown in Figure 3.21 indicate the locations of particles calculated by Michalke [18] under the same conditions with the Fortran code was run. Michalke [18] actually did not calculate the pathlines in his work. Instead of this, he calculated the streakline patterns, and marked the particles starting with constant time delay. Constant time delay equals to time period of the disturbance and at the beginning of each period, one particle is released into the flow. In other words, particles from different locations are released into the flow at $t_0 = mT$ where $(m = 0, \pm1, \pm2, \pm3, ..)$.

In Figure 3.21, the diamonds were obtained for one time period (i.e. locations of the first particles released at time $t = T$). Obviously, the Fortran code gives the same results with Michalke [18].

In order to see the initial formation of the instabilities, the pathlines are drawn along two times of the wavelength λ by the help of the periodicity of the flow. From Figures 3.22,3.23,3.24 and 3.25, the pathlines of the particles released from different locations at four different times can be seen.

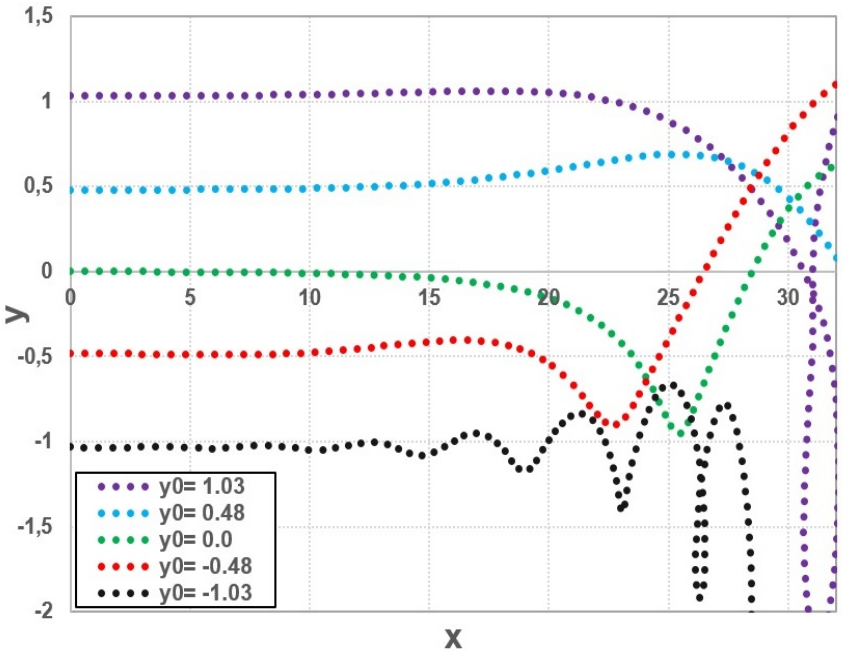

Figure 3.22: Pathlines of the particles released from different locations at $t = T$.

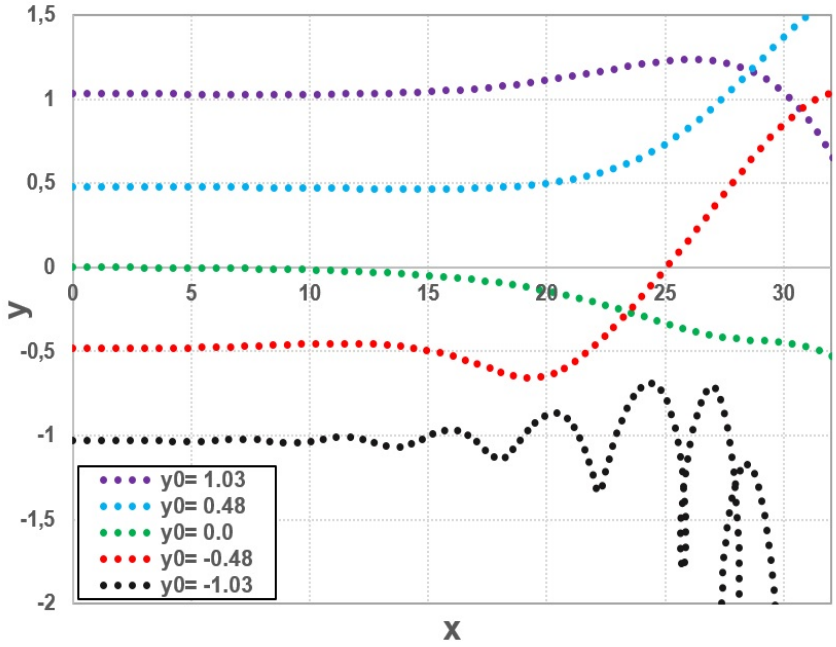

Figure 3.23: Pathlines of the particles released from different locations at $t = 1.25T$.

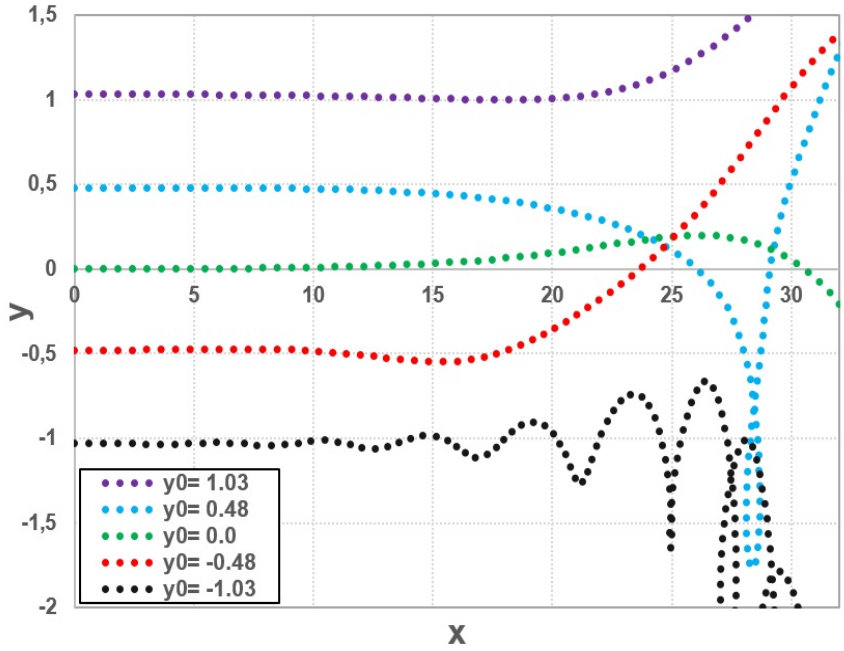

Figure 3.24: Pathlines of the particles released from different locations at $t = 1.5T$.

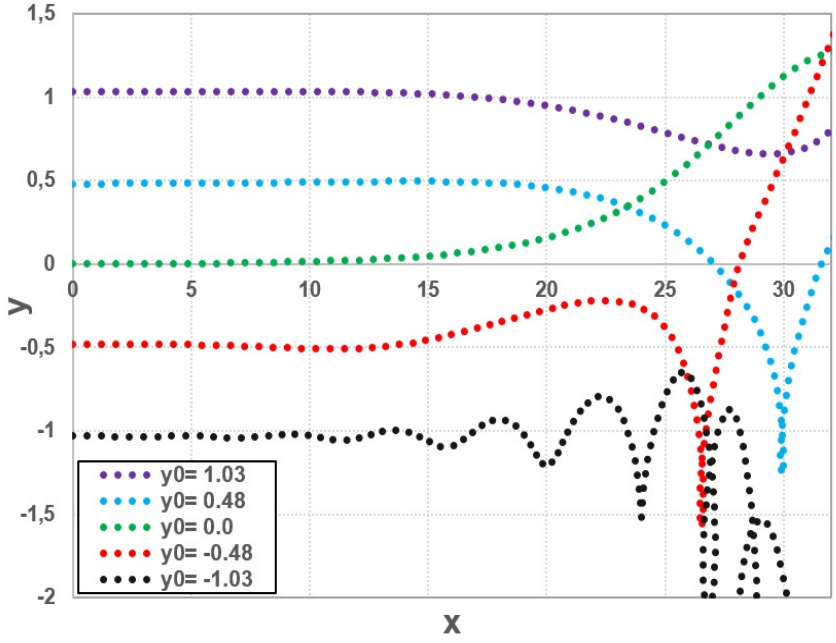

Figure 3.25: Pathlines of the particles released from different locations at $t = 1.75T$.

It is hard to make an inference from Figures 3.22,3.23,3.24 and 3.25, because the particles track tangled paths. However, it can be said that the particles in the upper region have a tendency to go down to the lower region of the shear layer in the beginning. By the time, this tendency changes to reverse direction.

The particles released from the bottom of the layer (i.e. $y_0 = -1.03$) makes an exception since they always moves down. The effects of the disturbances are observed the earliest on the particles released from the bottom. This is related to the highest disturbance velocity magnitudes of these particles in y-direction.

Streaklines provide cleaner pictures of the flow compared to the pathlines. They are related to the motion of the flow, not to the motion of particles in the flow. Therefore, in Figures 3.26, 3.27, 3.28 and 3.29, the streakline patterns of the disturbed shear flow are plotted for four different times.

Streaklines are obtained by using the calculations for the pathlines. To simulate the flow, time increment used for the release of the particles into the flow is choosen very small (i.e. $\Delta T = 0.1T$). By doing so, the particles become released just one after another making a continuous flow. Then the pathlines are calculated by integrating equation (2.119) in Section 2.4 from $t_0 = n\Delta t$ where $(n = 0, 1, 2, .., T/\Delta t)$ to $t = nT$. By connecting the end points of the pathlines, the streakline patterns shown in figures below are obtained.

Streaklines drawn in Figures 3.26, 3.27, 3.28 and 3.29 are easier to interpret compared to the pathlines shown in Figures 3.22, 3.23, 3.24 and 3.25. They reflect the motion of the flow clearly and continuously.

When the motion of the flow is investigated, it is seen that the streaklines have a tendency to roll up, since the particles starting originally in $y > 0$ region move to $y < 0$ region where they slow down. The streakline patterns are compatible with the calculations of the Michalke [18] and similar to the results of the experiments conducted by Freymuth [17].

The periodicity of the results obtained by the Fortran code are also checked. This

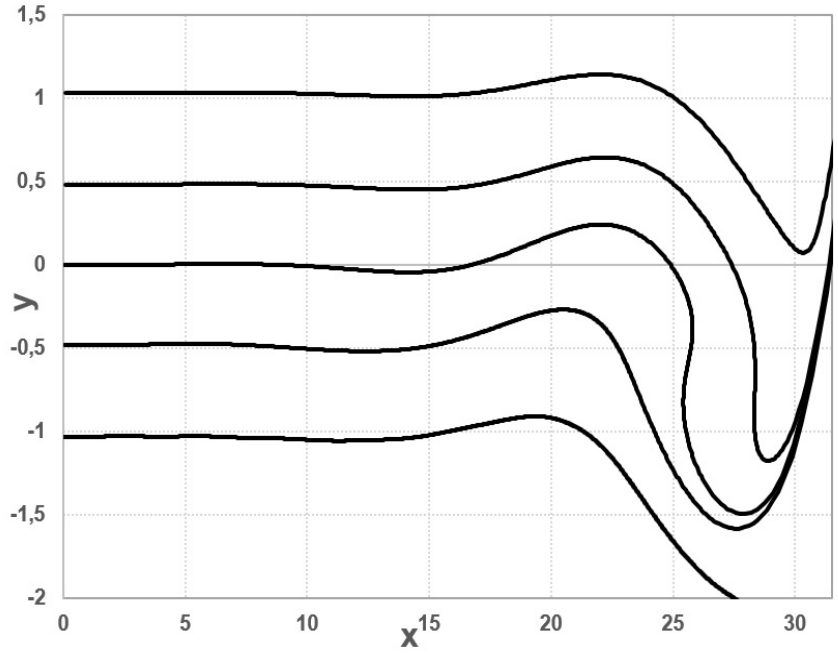

Figure 3.26: Streakline patterns of the flow at $t = T$.

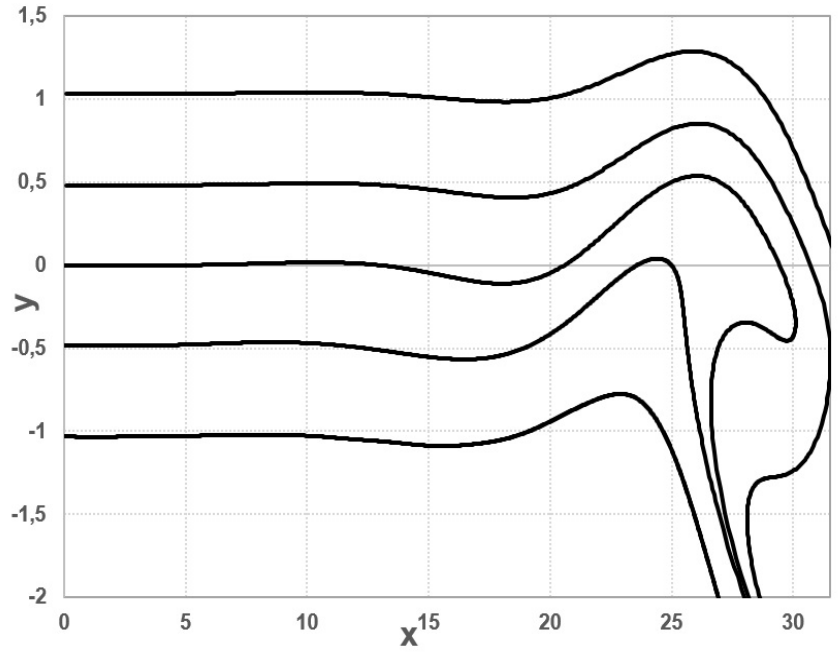

Figure 3.27: Streakline patterns of the flow at $t = 1.25T$.

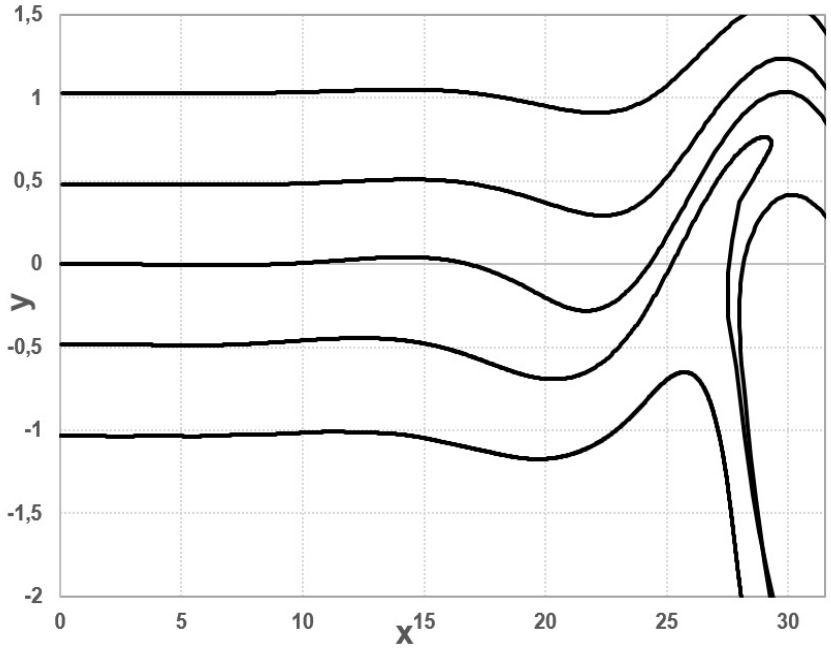

Figure 3.28: Streakline patterns of the flow at $t = 1.5T$.

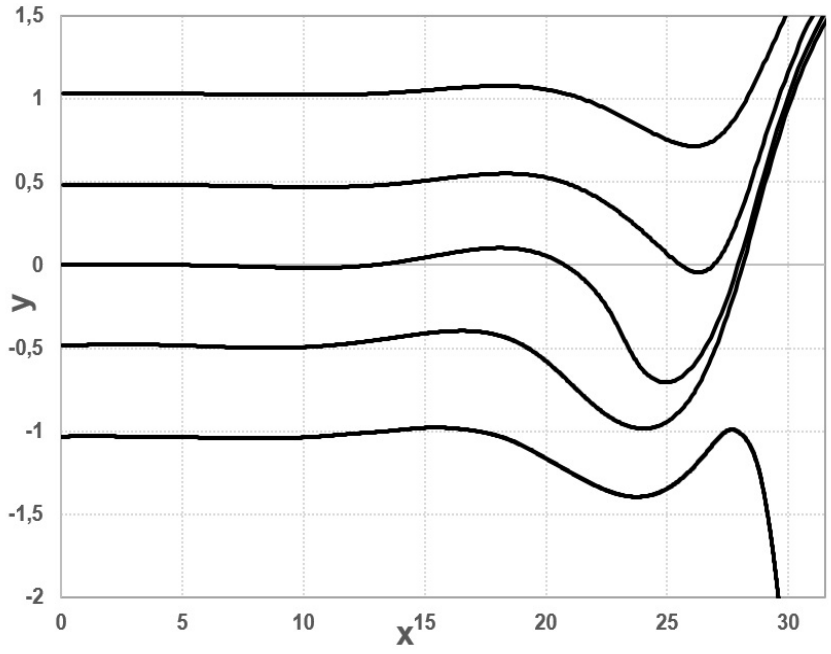

Figure 3.29: Streakline patterns of the flow at $t = 1.75T$.

is achieved by calculating the streaklines just before the end of second time period $t = 2T$. To make the differences between two streakline patterns more obvious, they are plotted at $t = 1.95T$ and $t = 2T$ as depicted in Figure 3.30. Clearly, at $t = 1.95$ the streakline pattern becomes very similar to one at $t = 2T$ as expected. Since the flow is periodic, the streaklines at $t = 2T$ have the same shape with the streaklines at $t = T$.

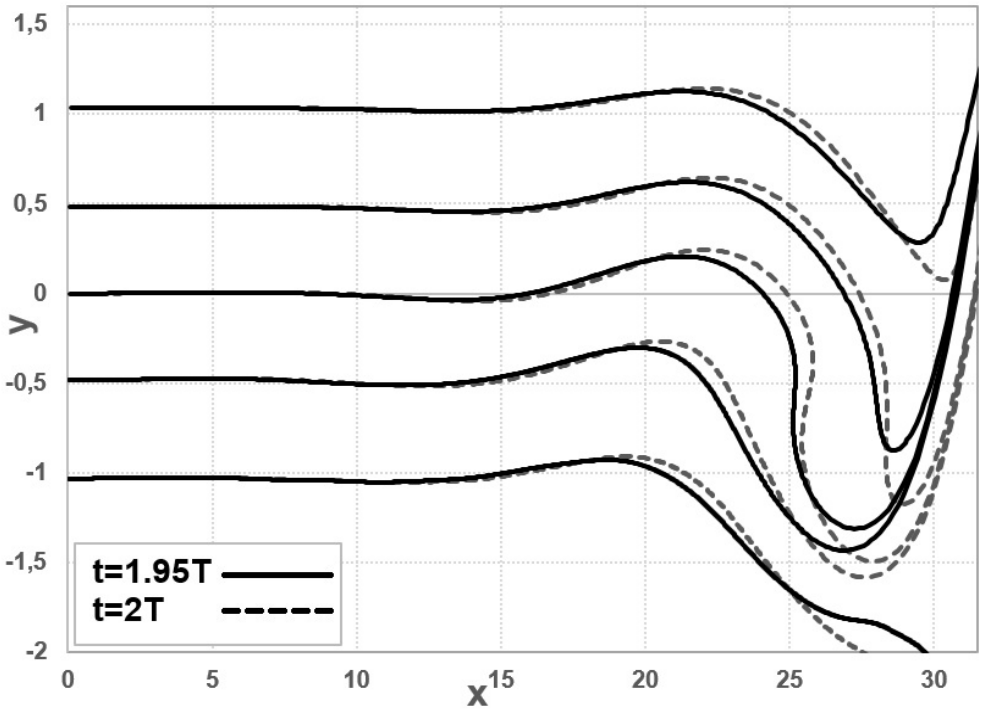

Figure 3.30: Streakline patterns of the flow at $t = 1.95T$ and $t = 2T$.

Streaklines are plotted for different disturbance frequencies other than $\beta = 0.2067$ at which, the disturbances grows rapidly. In Figures 3.31 and 3.32, streakline patterns for $\beta = 0.150$ and $\beta = 0.300$ are shown, respectively. Compared with streaklines for $\beta = 0.2067$ given in Figure 3.26, growth of the disturbances are slow for $\beta = 0.150$ and $\beta = 0.300$. This is normal, since the amplification rates of disturbances $alpha_i$, have lower values for $\beta = 0.150$ and $\beta = 0.300$.

The interesting point for the streaklines of different frequencies is that although at $\beta = 0.15$ and $\beta = 0.30$, amplification rates are almost equal, the disturbances grow

faster at $\beta = 0.30$ as seen from Figure 3.32. When this situation is investigated, it is seen that for beta=0.300, the wavenumber of the disturbances are higher which makes the growth of the disturbances faster. Therefore, it can be said that the wavenumber has also impact on the growth rate of the disturbances in shear layer.

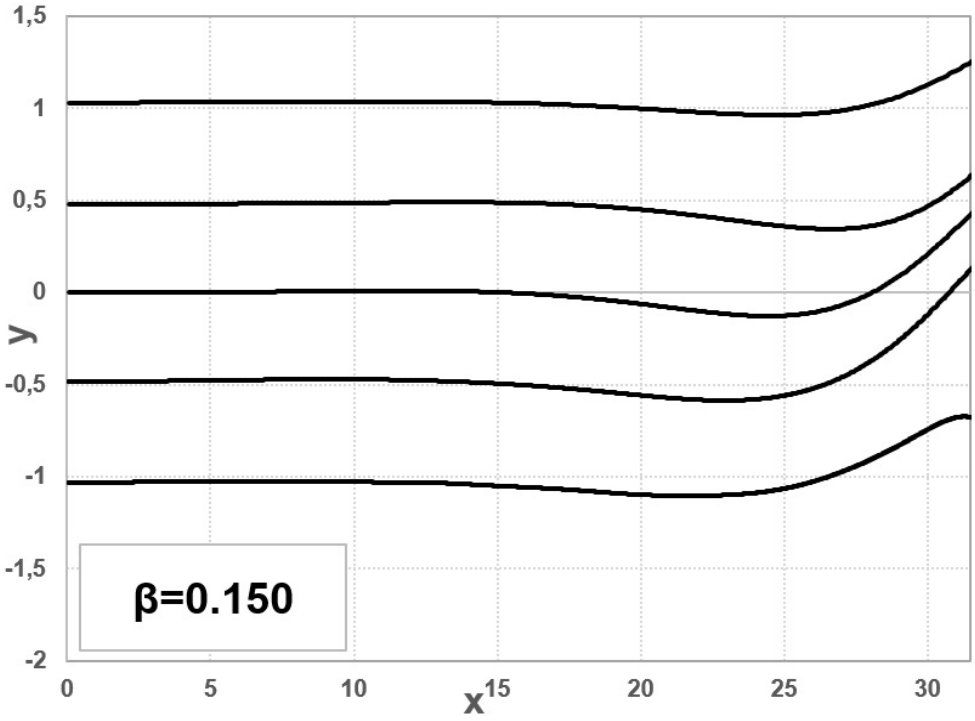

Figure 3.31: Streakline patterns of the flow at $t = T$ for $\beta = 0.150$.

Another important point for the calculation of the pathlines and the streaklines is that after almost two times of the wavelength of the disturbances, linear stability theory fails. After two times of the wavelength, the vorticity amplitudes and its derivatives attain very high values which can not be covered by the linear model. Since the disturbance velocity components are directly related to the vorticity amplitudes, calculation of them become impossible.

When the time performance of the Fortran code for the calculation of pathlines and streaklines is considered, it can be said that it is very fast while calculating pathlines. Figures 3.22,3.23,3.24 and 3.25 are plotted instantly after runnig the code. For streakline patterns, the run time of the code takes a little longer, since over 3000 pathlines

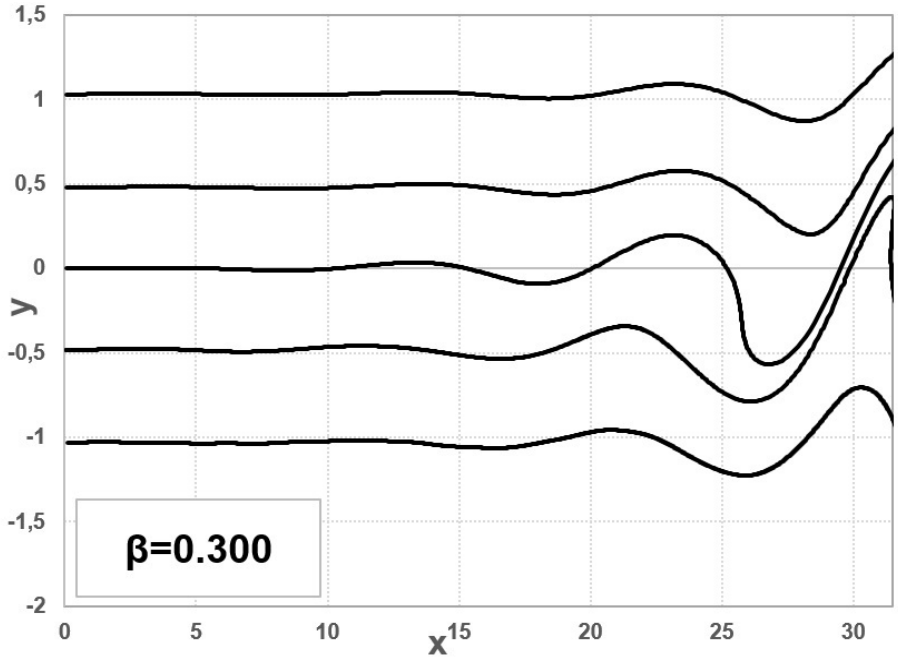

Figure 3.32: Streakline patterns of the flow at $t = T$ for $\beta = 0.300$.

are calculated for each t value. Specifically speaking, it takes about 4-5 minutes to plot a streakline pattern like the one given in Figure 3.26.

CHAPTER 4

DIFFERENT VELOCITY PROFILES

To test the capabilities of the developed Fortran Code, the different velocity profiles should be used. In the previous section, the code was validated for the hyperbolic tangent velocity profiles with temporal amplification approach. Therefore, in this section the velocity profiles derived from hyperbolic tangent velocity profile and parabolic velocity profiles are studied by the help of the code.

4.1 Hyperbolic Tangent Velocity Profile Family

In Figure 4.1, different versions of the hyperbolic tangent velocity profile investigated in previous section can be seen. These are the velocity profiles observed in the experiments of Freymuth [17], as the jet flow slows along the axial direction. With decrease in the flow velocity, the slope of the velocity profile also decreases.

In Figures 4.2 and 4.3, the real and imaginary parts of the eigenvalues calculated for hyperbolic tangent velocity profile family by using spatial amplification theory are shown.

When the amplification rates are examined, it can be said that with decrease in the slope of the velocity profile, the disturbance growth rate become smaller. Moreover, the flow become more stable, since the frequency range, in which disturbances grow, diminish. This means that with slower basic velocity, more stable flow can be obtained.

This makes sense in physical point of view. With decrease in the slope in the basic

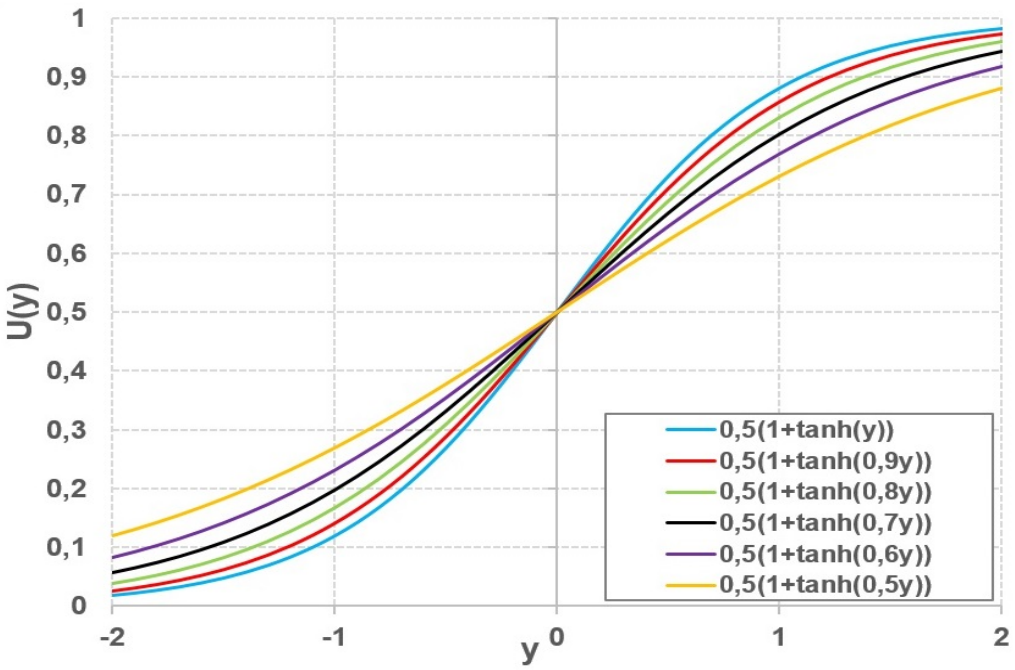

Figure 4.1: Hyperbolic Tangent Velocity Profile Family

flow, velocity gradients become slower, the vorticity get smaller. Since for the inviscid instability, the driving mechanism is the vorticity, the flow become stable. This principle can be used as flow control mechanism.

4.2 Capability of The Fortran Code for Parabolic Velocity Profiles

In Figure 4.4, the parabolic velocity profiles used by Ozgen & Uzol [21] are shown. They analyzed the velocity profiles for incompressible, inviscid, axisymmetric flows in cylindrical coordinates with temporal approach. To achieve this, they obtained a dispersion relation by applying the small disturbance theory followed by a normal mode analysis to the cylindrical momentum equations.

The parametrized equation of velocity profiles given in Figure 4.4 is given by equation (4.1), where b is the velocity profile parameter and varies between 0 for a uniform profile and 1 for a fully developed flow.

$$U(r) = 1 - br^2 \tag{4.1}$$

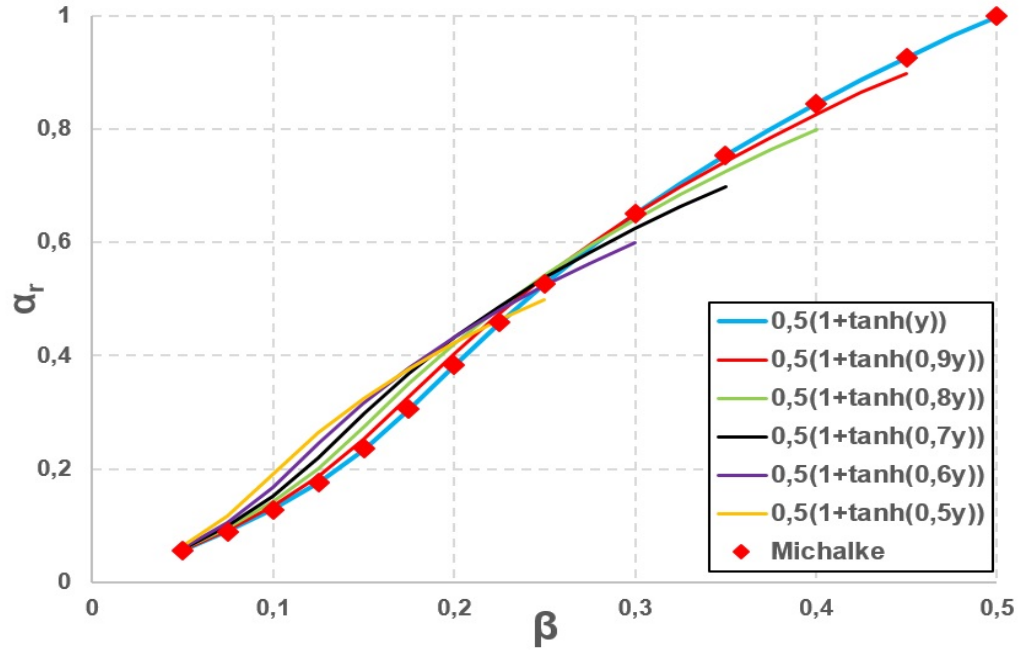

Figure 4.2: Real parts of eigenvalues for hyperbolic tangent velocity profile family

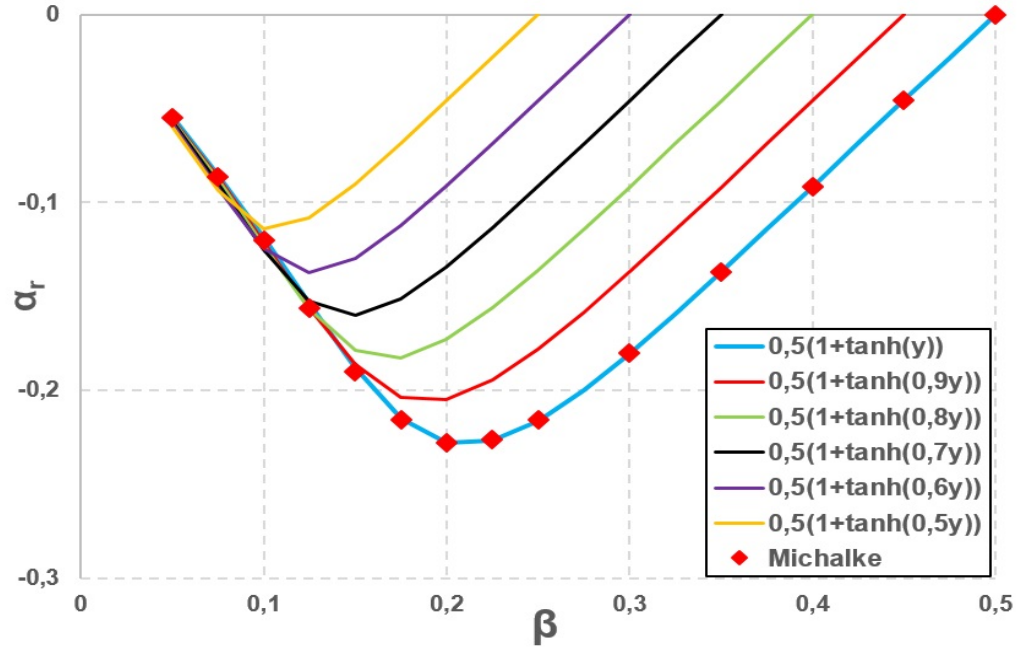

Figure 4.3: Imaginary parts of eigenvalues for hyperbolic tangent velocity profile family

In this thesis, the Fortran Code was developed from the Helmholtz's vorticity equation which is applicable for 2-D. Therefore, the parabolic velocity profiles given by equation (4.1) can be directy converted to the cartesian coordinates as;

$$U(y) = 1 - by^2 \tag{4.2}$$

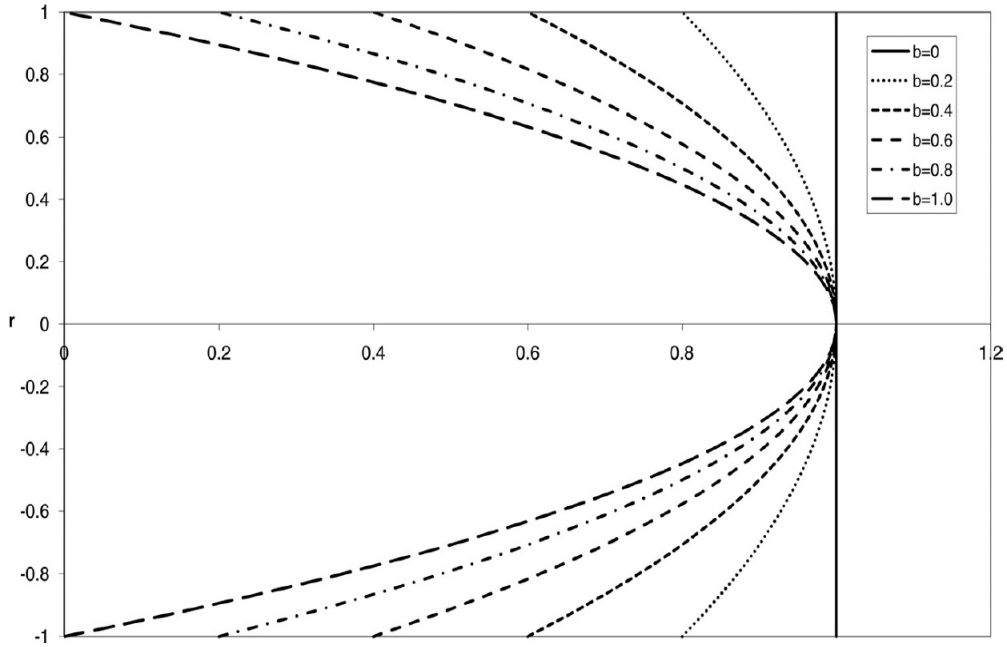

Figure 4.4: Parabolic velocity profiles.

The temporal version of the Ricatti equation given by equation (2.54) in Section 2.1, should be transformed by using the equation (4.2). The first and second derivatives of the equation (4.2) yields equations (4.3) and (4.4), respectively.

$$U' = -2by \tag{4.3}$$

$$U'' = -2b \tag{4.4}$$

By putting equations (4.2) and (4.4) to the temporal Ricatti Equation, the following equation is obtained, the boundary conditions of which does not change and given by Equation [101] in Section 2.1.

$$\frac{d\Phi}{dy} = \alpha^2 - \Phi^2 + \frac{-2b}{(1 - by^2 - i2c_i)} \tag{4.5}$$

To solve Equation (4.5), again $z = tanh(y)$ transformation was applied which is suitable to boundary conditions of the Ricatti Equation to solve numerically.

$$y = tanh^{-1}(z) \tag{4.6}$$

$$\frac{d\Phi}{dz} = \frac{d\Phi}{dy}\frac{dy}{dz} = \frac{\alpha^2 - \Phi^2}{1 - z^2} - \frac{2b}{(1 - b(tanh^{-1}(z))^2 - i2c_i)(1 - z^2)} \tag{4.7}$$

Equation (4.7) was used to calculate the eigenvalues with the method mentioned in sections 2.1 and 2.2. For the eigenvalue calculations two modes were examined as Ozgen & Uzol [21] did. First wheter the code was capable to give a solution in atomization regime was checked. It was seen that in the atomization instability mode (i.e. $\alpha \gg 1$), the code did not yield any eigenvalues for different velocity profile parameters. This is an expected result, since the code was designed by Rayleigh equation which is valid for Rayleigh regime (i.e. $\alpha < 1$).

Secondly, the performance of the code was tested in Rayleigh regime. Although Serkan & Uzol [21] had results in this regime for $b = 0.2$, the code developed could not calculate the eigenvalues for the same $b = 0.2$. When the different parabolic velocity profiles were examined, it was observed that the code did not work properly. For example, for $b = 0, 0.1, 0.2, 0.3, 0.4, 0.5$ the code did not calculate any eigenvalues.

It was understood that the Fortran code developed was not capable to analyze the parabolic velocity profiles, when the runs with these velocity profiles were investigated. Then, the root causes of this failure were researched to determine whether the algorithm of the code was wrongly established for the parabolic velocity profiles.

Ozgen & Uzol [21] obtained result for the parabolic velocity profile in the Rayleigh instability regime. They used the cylindrical momentum equations to obtain dispersion relation and by the help of it they could calculate the eigenvalues. Therefore, the main difference of the Fortran code is the equation on which the code depends.

The most unstable case for the parabolic velocity profiles is the uniform flow. equa-

tion (4.7) re-written for the uniform flow ($b = 0$) is shown below.

$$\frac{d\Phi}{dz} = \frac{\alpha^2 - \Phi^2}{1 - z^2} - \frac{2 \times 0}{(1 - 0 \times (tanh^{-1}(z))^2 - i2c_i)(1 - z^2)} = \frac{\alpha^2 - \Phi^2}{1 - z^2} \tag{4.8}$$

With the boundary conditions $\Phi(z_b) = -z_b\alpha$, equation (4.7) yields 0, which is our search criteria for the eigenvalues of the temporal Ricatti Equation. Therefore, no matter α value takes, at the first iteration of the eigenvalue search criteria is already satisfied. Thus, instead of wrongly coding, it can be said that the mathematical model (Rayleigh Equation) causes the problem which will be discussed in the next section.

4.3 Discussion on the Rayleigh Instabilities

The boundary layers or shear layers are unstable when $c_i > 0$. Taking this criteria into consideration, by re-arranging the terms of the temporal Rayleigh equation and multiplying it with the complex conjugate of ϕ, the following equations are obtained.

$$\frac{d\phi^2}{d^2y} - \Big(\alpha^2 + \frac{U''}{U - c}\Big)\phi = 0 \tag{4.9}$$

$$\bar{\phi}\frac{d\phi^2}{d^2y} - \Big(\alpha^2 + \frac{U''}{U - c}\Big) \mid \phi \mid^2 = 0 \tag{4.10}$$

Integrating equation (4.9) from y_1 to y_2 with respect to y, where y_1 or y_2 is finite for boundary layers and the both are infinite for shear layer;

$$\int_{y_1}^{y_2} \bar{\phi}\frac{d\phi^2}{d^2y}dy - \int_{y_1}^{y_2} \Big(\alpha^2 + \frac{U''}{U - c}\Big) \mid \phi \mid^2 dy = 0 \tag{4.11}$$

Where $\mid \phi \mid^2 = \phi\bar{\phi}$. Integrating the first term of equation (4.10) by parts;

$$\Big[\frac{d\phi}{dy}\bar{\phi}\Big]_{y_1}^{y_2} - \int_{y_1}^{y_2} \frac{d\phi}{dy}\frac{d\bar{\phi}}{dy}dy - \int_{y_1}^{y_2} \Big(\alpha^2 + \frac{U''}{U - c}\Big) \mid \phi \mid^2 dy = 0 \tag{4.12}$$

First term of the equation above equals to zero, since $\bar{\phi}(y_1) = \bar{\phi}(y_2) = 0$. By multiplying th denominator and the numerator of the second term with $U - \bar{c}$ the equation becomes;

$$-\int_{y_1}^{y_2} \mid \frac{d\phi}{dy} \mid^2 dy - \int_{y_1}^{y_2} \Big(\alpha^2 + \frac{d^2U/dy^2(U - \bar{c})}{\mid U - c \mid^2}\Big) \mid \phi \mid^2 dy = 0 \tag{4.13}$$

Where $\bar{c}$ is complex conjugate of c. The imaginary part of equation (4.13) is;

$$-c_i \int_{y_1}^{y_2} \frac{d^2U/dy^2 \mid \phi \mid^2}{\mid U - c \mid^2} dy = 0 \tag{4.14}$$

Since $c_i > 0$ for unstable flow as assumed at first, the integral I should be equal to zero to satisfy the equation above. Since the terms $\mid \phi \mid^2$ and $\mid U - c \mid^2$ are also greater than zero, d^2U/dy^2 term remains to be zero which means that d^2U/dy^2 should change its sign in the region (y_1, y_2).

The derivation mentioned above is known as Rayleigh's inflection theorem, which briefly defines the necessary condition for inviscid instability as the presence of an inflection point in the velocity profile. According to the theorem, the absence of an inflection point necessarily confers inviscid stability.

For the parabolic velocity profiles defined by equation (4.2), d^2U/dy^2 does not change its sign in any domain and equals to $-2b$, meaning that they are stable. Therefore, it makes sense that Rayleigh Equation does not yield any eigenvalue for the disturbance growth, since the parabolic velocity profiles are already stable according to the inflection theorem.

CHAPTER 5

CONCLUSION & FUTURE WORK

In this thesis, an in house Fortran Code developed to investigate the spatial and temporal instabilities for inviscid shear layer by the linear stability theory. To establish the mathematical model on which the code depends on Rayleigh and Ricatti equations were derived from the Helmholtz vorticity equation by utilizing the small and wavy disturbances. For the hyperbolic-tangent velocity profile, the transformed Ricatti equation was solved by using space and time amplification approaches by an in-house Fortran Code involving Runge-Kutta-Gill and simplex method algorithms.

By using the Fortran Code developed, eigenvalues of various disturbance frequencies were calculated for both spatial and temporal amplification. It was seen that the eigenvalues and the amplification rates obtained by the code were totally matching with the literature. Then, the results of two theories were compared and the most strongly amplified disturbance frequencies were evaluated. For the lower disturbance frequencies, it was observed that calculations of the spatial theory were more reliable, since they were closer the experimental results.

Eigenfunctions of spatial theory were plotted for various disturbance frequencies. For the most strongly amplified disturbance frequency, eigenfunctions were calculated for both theories and compared. In spatial amplification case, derivatives of the eigenfunctions were drawn and evaluated. Again, it was understood that the spatial amplification model reflects the instability mechanism because it can model the phase reversal phenomena observed in the experiments.

By using the post-proccessing tools of the Fortran Code, the vorticity amplitudes were also calculated for different disturbance frequencies and validated with the results in

the literature. Then, constant vorticity distributions of spatial amplification case were plotted at different times in order to demonstrate the mechanism of instability.

At the most strongly amplified disturbance frequency of spatial theory, the motion of particles at the different locations in the shear layer were investigated by drawing the pathlines and the streaklines of them. The results for the pathlines were verified by the calculations done in the past. When the pathlines and the streaklines were evaluated, it was seen that the streaklines patterns gave more clear images of the instability mechanism occurring in the shear layer.

The streaklines patterns at the different disturbance frequencies were plotted, also. It was seen that before and after the most strongly amplified disturbance frequency, growth of the disturbances are slower, as expected. Moreover, it is seen that wavenumber has also an impact on the disturbance growth rate, when the streaklines at different frequencies with same amplification rates are examined.

The code was run with the hyperbolic tangent velocity profile family and parobolic velocity profiles to test its limits. It was seen that for the hyperbolic tangent velocity profile family, with slower basic velocity, more stable flow was obtained. For the parabolic velocity profiles, the code failed. The reason why the code was not capable to analyze the inviscid parabolic velocity profiles were discussed. The mathematical base of the code was main reason of the failure for the parobolic velocity profiles. Rayleigh equation on which the code depends, directly resulted in satisfied stability criteria since the parabolic velocity profiles did not have inflection points. Therefore, by using it could not be possible to get the disturbance amplification rates which could be calculated by the dispersion relation obtained from the momentum equations.

For the future studies, the gap in the code for the calculations of the parabolic velocity profiles can be tried to be fulfilled. This can be done by adding the dispersion relation feature based on Navier-Stokes equations. Moreover, by using Navier-Stokes equations, the effect of pressure can also be implemented to the code, however, it should be noted that this will need much more things to do compared to incompressible case.

REFERENCES

[1] I. Tani, "History of boundary-layer theory," *Ann. Rev. Fluid Mech*, vol. 9, pp. 87–111, 1977.

[2] P. J. Pritchard and J. C. Leylegian, *Fox and McDonald's Introduction to Fluid Mechanics*. Danvers, Massachusetts: John Wiley & Sons, Inc., 2011.

[3] H. Schlichting, *Boundary Layer Theory*. McGraw-Hill Book Co. Inc., 1979.

[4] H. L. Reed and W. S. Saric, "Linear stability theory applied to boundary layers," *Ann. Rev. Fluid Mech*, vol. 28, pp. 389–428, 1996.

[5] L. Rayleigh, "Science papers," *Cambridge University Press*, vol. 1, pp. 474–487, 1880.

[6] M. Lessen, "On stability of free laminar boundary layer between parallel streams," *Nat. Adv. Comm. Aero. Tech. Rep.*, vol. 979, 1950.

[7] R. E. Esch *International Journal of Fluid Mechanics*, vol. 3, pp. 289–303, 1957.

[8] R. Betchov and A. Szewczyk *The Physics of Fluids*, vol. 6, pp. 1391–1396, 1963.

[9] T. Tatsumi and T. Kakutani, "The stability of a two-dimensional laminar jet," *International Journal of Fluid Mechanics*, vol. 4, pp. 261–275, 1958.

[10] H. Sato, "The stability and transition of a two-dimensional jet," *International Journal of Fluid Mechanics*, vol. 7, 1959.

[11] V. A. Michalke and H. Schade, "Zur stabilitiit yon freien grenzschichten," *Ingenieur Archiv*, vol. 33, 1963.

[12] V. A. Michalke and R. Wille, "Strmungsvorgnge im laminar-turbulenten bergangsbereich von freistrahlgrenzschichten," *Proc. of 11th International Congress of Applied Mechanics*, p. 962, 1965.

[13] H. Sato, "Experimental investigation on the transition of laminar seperated layer," *Journal of the Physical Society of Japan*, vol. 11, 1956.

[14] H. Sato, "Further investigation on the transition of two-dimensional seperated layer at subsonic speeds," *Journal of the Physical Society of Japan*, vol. 14, 1959.

[15] O. Wehrmann and R. Wille, "Beitrag zur phanomenologie des laminar-turbulenten ubergangs im freistrahl bei kleinen reynoldszahlen," *Boundary Layer Research*, pp. 387–407, 1958.

[16] V. A. Michalke, "On the inviscid instability of the hyperbolic tangent velocity profile," *International Journal of Fluid Mechanics*, vol. 19, 1964.

[17] P. Freymuth, "On transition in a separated laminar boundary layer," *International Journal of Fluid Mechanics*, vol. 25, pp. 683–704, 1966.

[18] V. A. Michalke, "On spatially growing disturbances in an inviscid shear layer," *International Journal of Fluid Mechanics*, vol. 23, 1965.

[19] H. Yang and Y. Zhou, "Axisymmetric jet manipulated using two unsteady mini-jets," *International Journal of Fluid Mechanics*, vol. 808, pp. 362–396, 2016.

[20] F. Liu, Y. Wang, and Y. Piao, "Linear stability analysis of interactions between mixing layer and boundary layer flows," *Chinese Journal of Aeronautics*, vol. 30, pp. 1327–1335, 2017.

[21] S. Ozgen and O. Uzol, "Investigation of the linear stability problem of electrified jets, inviscid analysis," *Journal of Fluids Engineering*, vol. 134, 2012.

[22] W. T. V. William H. Press, Saul A. Teukolsky and B. P. Flannery, *Numerical Recipes in Fortran 77: The Art of Scientific Computing (Vol. 1 of Fortran Numerical Recipes)*. Melbourne, Australia: The Press Syndicate of the University of Cambridge, 1997.